Emergence of growth and dormancy from a kinetic model of the *Escherichia coli* central carbon metabolism

Yusuke Himeoka ◉

Universal Biology Institute, University of Tokyo, 7-3-1 Hongo, Bunkyo-ku, Tokyo, Japan

Namiko Mitarai ◉

The Niels Bohr Institute, University of Copenhagen, Blegdamsvej 17, Copenhagen, 2100, Denmark

Physiological states of bacterial cells exhibit a wide spectrum of timescale. Under nutrient-rich conditions, most of the cells in an isogenic bacterial population grow at certain rates, while a small subpopulation sometimes falls into a dormant state where the growth rates slow down by orders of magnitude. The dormant cells have unique characteristics: The metabolic activity is quite slow, and the dormant cells typically exhibit a high tolerance for a range of stresses, such as antibiotics applications. To reveal the origins of such heterogeneity of timescales, we constructed a kinetic model of *Escherichia coli* central carbon metabolism, including the dynamics of the energy currency molecules, and asked if perturbations of the metabolites' concentrations lead to the distinct metabolic states. By numerically studying the relaxation dynamics, we found that the model robustly exhibits two qualitatively distinct relaxation dynamics depending on the initial conditions generated by the perturbations. In the first type, the concentrations of metabolites reach the steady state quickly, resembling the growing dynamics. On the other hand, the other type of dynamics takes a much longer time to reach the steady state, and during the relaxation, cell growth almost halts, reminding us of the dormant cells. In order to unveil the mechanism of distinct behaviors, we reduced the metabolic network model into a minimal model without losing the emergence of distinct dynamics. Analytical and numerical studies of the two-variable minimal model revealed the necessary conditions for the distinct behavior, namely, the depletion of energy due to the futile cycle and its nonuniform impact on the kinetics because of the coexistence of the energy currency-coupled and uncoupled reactions as well as branching of the network. The result is consistent with the experimental reports that the dormant cells commonly exhibit low ATP levels and provides a possible explanation for the appearance of dormant cells that causes antibiotic persistence.

I. INTRODUCTION

Bacterial growth rates span a wide range of timescales: *Escherichia coli* cells typically double every 20 minutes under nutrient-rich conditions, while cells can also exhibit dormancy where the growth of cells almost halts and yet the death is strongly suppressed [1–3]. The transition to the dormant states can either be a stochastic event or a response to hostile environments such as starvation and exposure to antibiotics. This dormancy is a beneficial strategy for surviving nutrient-poor conditions as it can lower the cell's nutrient requirements [4]. Also, dormancy is known as the main cause of bacterial persistence that has a high tolerance to antibiotics, and thus, has been gathering attention from a wide range of fields from microbiology to therapeutic studies [2,3,5,6].

Notable changes in the timescale of cellular physiology are happening in the dormant cells. It has been implied that the dormant cells have a sort of memory capacities: The lag time was shown to depend on the length of time that the cells are starved [7–9] and the death rates of the starved cells differ depending on the previous culture conditions even though the starvation condition is identical [10]. Given that slow dynamics are vital for storing memories, a drastic change in the timescale of cellular physiology is necessary. Indeed, it was reported that the proteome kept changing at least for 8 hours in the starved *E. coli* cells [11].

Experimental studies have revealed the links between dormancy and several molecules, such as growth-inhibiting genes and metabolic enzymes (cf. reviews of Refs. [3,12,13]). Based on the experimental findings, models that exhibit the transition to dormancy have been proposed. The model developed by Klumpp *et al.* [14] shows the bistability of growing- and dormant state led by the toxin-based feedback mechanism of gene expression. The transition mechanism suggested by Rocco *et al.* is based on the bursting activity of gene expression [15,16]. According to the model by Radzikowski *et al.* [11], the collapse of the metabolic homeostasis by perturbation is the key to the transition: A strong perturbation is applied to the

metabolic state, and the resulting low metabolic flux cannot support the synthesis of the metabolic enzymes to restore metabolic homeostasis. This failure of metabolic readjustment further lowers metabolic activity.

All the models mentioned above for exhibiting the dormancy transition include the gene expression dynamics. Here in the present paper, we explored another possibility: the dormancy transition is triggered by the metabolic dynamics itself, without regulatory changes. Metabolic reaction networks are highly interconnected via cofactors such as ATPs; thus, the kinetic models of metabolic networks should have high nonlinearities. The emergence of different timescales is one of the hallmarks of nonlinear dynamical systems. Indeed, the studies of a simple catalytic reaction network showed that the relaxations to the steady state are much slower than that inferred from the rate constants of the reactions and exhibit multiple plateaux [17–19].

In the present paper, we study the kinetic model of *E. coli* central carbon metabolism with cofactors, such as ATP, as variables. There are a number of studies of kinetic model of *E. coli* central carbon metabolism [20–35]. However, as far as we know, the dynamics of the cofactors are often neglected [20–30], or if included, the relaxation dynamics of the models are not actually computed [31–35]. As the experimental studies suggested [36,37], ATPs may play a central role in the transition to dormancy. Thus, the cofactors can be vital model components for studying the growth-dormancy transition.

In the following sections, we present that the kinetic model of *E. coli* central carbon metabolism with cofactors robustly exhibits two distinct dynamics: One is reminiscent of the normal growth behavior, and the other is analogous to the dormant dynamics. Then we derive the minimal network showing qualitatively the same dynamics. The minimal model analysis reveals two necessary conditions for the emergence of both growth and dormant dynamics: the depletion of energy due to the futile cycle and its nonuniform impact on the kinetics because of the coexistence of the energy currency-coupled and uncoupled reactions as well as branching of the network.

The obtained result implies that the depletion of ATP and ADP itself leads to the slow dynamics of the metabolites' concentrations. This conclusion is consistent with the "low-energy" view of the bacterial dormancy presented in [36,38], and highlights the notable impact of introducing cofactors into models. We also discuss the possible applications of our analysis for the studies of dormancy in other species based on the minimal network motifs.

II. MATERIALS AND METHODS

A. Simulation of ordinary differential equations (ODEs)

All the ODE computations were performed by using Matlab (Mathworks) `ode23s` function. For searching attractors, we set $10^{u_{i,n}}$ for the ith metabolite as the nth initial value where $u_{i,n}$ is the random number generated from a uniform distribution in $[-1, 1]$. The steady-state concentration $[X_i^{(ss)}]$ is then obtained, and initial concentrations for the main analysis of the dynamics are generated as $10^{u_{i,n}}[X_i^{(ss)}]$ with $u_{i,n}$ is the same random number yet distributed in $[-2, 2]$. The ODEs were computed with two tolerance options (`AbsTol` =

10^{-10}, `RelTol` = 10^{-12}) and (`AbsTol` = 10^{-10}, `RelTol` = 10^{-14}) from exactly the same initial points. After the computation, the trajectories with two different `RelTol` values, but from the same initial point, were compared for the quality check of the computation. If the Hausdorff distance of the pair of the trajectories was less than 0.5, the trajectories were considered as correctly computed, and the trajectory obtained with `RelTol` = 10^{-14} was used for the further analysis, and otherwise, discarded. The quality check of the computation was performed after the transformation $x(t) \to \ln(x(t))$ where $x(t)$ is the concentration of the chemicals.

B. Principal component analysis

We used the python package `sklearn.decomposition.PCA` [39] without whitening. The whitening leads to only a minor effect on the results. The concentrations of the chemicals were transformed into the natural logarithm of the concentration before the analysis. PCA is performed for each model, i.e., all the data points generated by a single model with a number of initial conditions (the state vectors representing the chemical concentrations) are stacked into a single dataset, and we computed the covariance matrix of the dataset for the projection of the trajectories.

III. RESULTS

A. Model

In the present paper, we study the *E. coli* core network [40] as one of the simplest models of the real metabolic reaction networks. The *E. coli* core model was obtained from BiGG database [41]. The model contains stoichiometry and the reversibility of the reactions. The *E. coli* core model has 52 and 75 intracellular metabolites and reactions, respectively. After an appropriate data curation as described later, we implemented the model by using the ordinary differential equation (ODE) that describes the dynamics of concentrations of metabolites.

We applied several modifications to the model to make it suitable for ODE implementation. First, small molecules such as O_2, H_2O, and NH_4, were not considered as variables but treated as constants under the assumptions that the external concentration of these chemicals are kept constant, and uptakes/secretions of them take place quickly. The uptake and secretion pathways of all carbon sources except glucose are removed.

Under anaerobic conditions, cells transfer the free energy to ATP directly, while under aerobic conditions, most of the energy transfer takes an indirect form: The energy is first transferred to other chemicals such as NADH and NADPH, and then, the stored energy in NADH, NADPH, and others are used for converting ADP to ATP. The conversion yield of ATP per NADH in the *E. coli* core model is 1.25 (via NADH16, CYTB, and ATPS4r), and NADH/NADPH yield is roughly unity. For introducing the cofactors to the model in a simple manner, we assume that the energy transfers via NADH and NADPH are sufficiently fast and ATP/NADH(NAPDH) yield as unity. According to these assumptions, we replace NAD(NADP) and NADH(NADPH) with ADP and ATP, respectively (we discussed the validity of this assumption in the
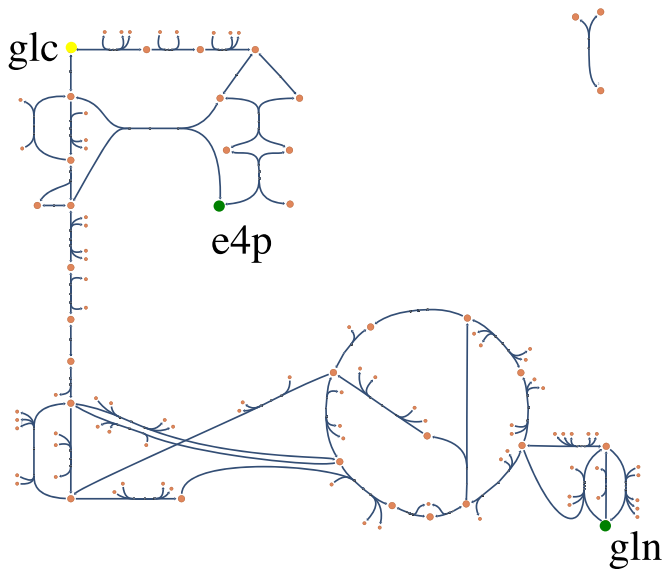
FIG. 1. The metabolic network of the *E. coli* core model generated by Escher [41]. The sole carbon source (glucose-6-phosphate) is placed at the left top (abbreviated as glc). We highlighted the substrates of the growth reaction other than ATP, namely, e4p and gln. The growth reaction is not drawn.

Sec. IV and Appendix F). Full lists of the chemical components and the reactions are provided in *SI Data*.1 within the Supplemental Material [42].

Also, the stoichiometry of the growth reaction was modified. The original *E. coli* core model has the biomass production reaction leading to the cell growth consisting of 16 substrates and 7 products with noninteger stoichiometry constants. For kinetic modeling, such reactions having too many substrates and products lead to numerical instability, and noninteger stoichiometry is unreasonable. Thus, we replaced the biomass production reaction with a following reaction: (erythrose 4-phosphate) + (L-glutamine) + (ATP) → (ADP). This reaction is much simpler than the original one. Still, it requires the model to run all the modules of the metabolic reactions, namely the pentose phosphate pathway for erythrose 4-phosphate (e4p), TCA cycle for L-glutamine (gln), and energy generation for ATP. Hereafter, we call this simplified biomass production reaction as the growth reaction.

The resulting model consists of 32 variables and 40 reactions. The final metabolic reaction network is drawn in Fig. 1. Our model cell takes up the nutrient from the node labeled as "glc", which has a constant concentration, performs successive conversion of the chemicals generating energy, and proceeds with the growth reaction.

First, we simulated the model with realistic setups. The kinetic parameters of *E. coli* core model have been estimated using the metabolic ensemble modeling (MEM) by Khodayari and colleagues [33]. We derived the Michaelis-Menten type rate equation for each reaction according to the enzyme kinetics used in [33] with the presented kinetic parameters. Then we assumed that each chemical species is consumed/synthesized by associated reactions, diluted as the cell grows, and spontaneously degraded at a slow rate. Thus, the temporal change of the concentration of the *i*th chemical

species X_i is ruled by

$$\frac{d[X_i]}{dt} = \sum_j S_{ij} J_j - d[X_i] - \mu[X_i], \qquad (1)$$

where S is the stoichiometric matrix, and J_i's are the fluxes due to chemical reactions. d and μ are the spontaneous degradation rate and the growth rate, respectively. Note that the concentrations of enzymes are supposed to be constant and lumped in the kinetic parameters. We assumed that spontaneous degradation is a very slow process represented by a single parameter. The dilution and degradation terms are omitted in the AMP, ADP, and ATP equations because the *de novo* synthesis of the adenine nucleotide carriers is not modeled in the *E. coli* core model. This assumption is equivalent to the homeostasis of the total adenine nucleotide carriers. (We check that the assumption can be relaxed by introducing a phenomenological reaction for the de-novo synthesis of AMP, see Appendix E). According to the growth reaction which we have introduced above, our model cell grows as the reaction (erythrose 4-phosphate) + (L-glutamine) + (ATP) → (ADP) proceeds. We chose the simplest kinetics of the growth reaction given by $J_g = v_g[\text{e4p}][\text{gln}][\text{atp}]$ and the growth rate as $\mu = rJ_g$. We fit the values v_g and r so that the growth rate at the steady state is in the range of the typical growth rate of *E. coli* in minimal glucose media ≈0.5 per hour. The spontaneous degradation rate d is set to be one-hundredth of the steady growth rate so that the effect of the spontaneous degradation is negligible at the attractor. The concentration of the nutrient ([glc]) and the total concentration of the adenine nucleotide carriers (A_t) are set to 20 mM and 1 mM, respectively (see Appendix A).

To see how many attractors the model has, we computed the model dynamics from multiple initial concentrations. As far as we have checked, the model has only a single steady-state attractor.

B. Dormant trajectory

We applied random perturbations to the steady-state concentration to emulate the exposure to the sublethal stresses that disturb intracellular states. The perturbations are applied in a multiplicative manner. For the metabolite i with the steady-state concentration $[X_i^{(\text{ss})}]$, the initial concentration is given by $10^u[X_i^{(\text{ss})}]$, where u is a random number sampled from uniform distribution in $[-2, 2]$. The concentrations of ATP, ADP, and AMP are normalized so that the total concentration is A_t because it is conserved in the model.

We found that the model exhibited two qualitatively distinct relaxation behaviors depending on the initial conditions. The typical time course of each type is plotted in Fig. 2(a) in log scale to depict the wide range of the concentration and timescale [43].

Even though the two trajectories eventually relax to the same steady state, the relaxation behaviors are evidently distinct. First, the concentrations after minutes (∼10^{-1} hours) are different between the top and bottom panels by many orders of magnitude. The concentrations of several chemicals are smaller than one molecule per cell, especially in the bottom panel. We revisit this point in the discussion section. Also,
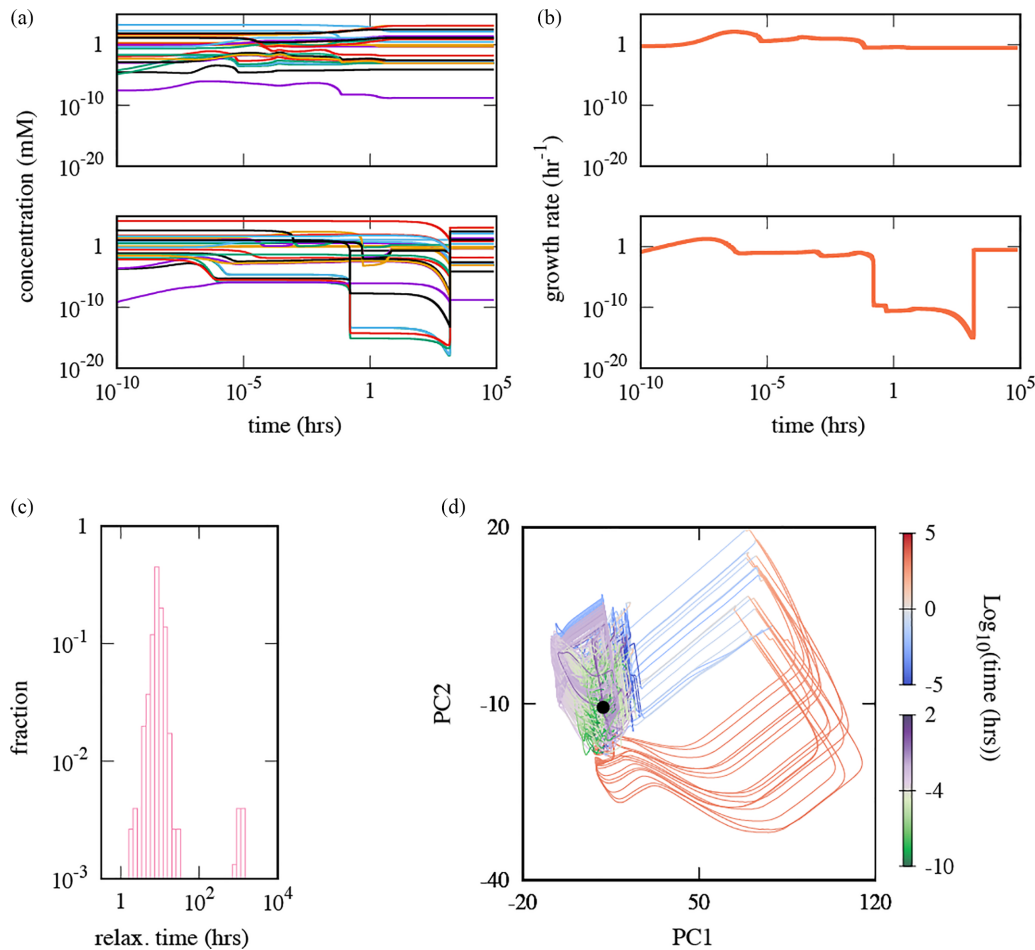
FIG. 2. (a) Two characteristic dynamics of *E. coli* core model starting from different initial points. While the growth rate of the cell is ≈ 0.5 per hour at the attractor, there are huge differences in the relaxation behaviors between the top and bottom panels. (b) The temporal changes of the growth rates along the dynamics in the same row in (a) are plotted. (c) The distribution of the relaxation time shows a clear bimodality. (d) Trajectories are overlaid in two-dimensional principal component space. The color indicates $\log_{10}$ of time. The trajectories having shorter relaxation time (several hours) are colored green-white-purple while the others are colored blue-white-red. The black point corresponds to the steady-state attractor. Initial concentration of each metabolites is $10^u [X_i^{(ss)}]$ mM with $[X_i^{(ss)}]$ as the steady-state concentration of the *i*th metabolite, and *u* as a random number uniformly distributed in $[-2, 2]$ while the total concentrations of adenine nucleotide carriers are normalized. Parameters other than ones obtained from [33] are $[glc] = 20$ mM, $A_t = 1$ mM, $d = 5 \times 10^{-3}$ h^{-1}, $v_g = 3.6 \times 10^4$ mM^{-2} sec^{-1}, and $r = 5.0$ mM^{-1}.

the characteristic timescale between them is clearly different. The concentrations of the chemicals reach close to the steady values in minutes in the top panel.

In contrast, the concentrations keep changing for a much longer time, $t \approx 10^3$ hours in the bottom panel, which is experimentally indistinguishable from the situation where cells stop growing. When sampled over various initial conditions, the relaxation time distribution has a clear bimodality as shown in Fig. 2(c). Here, the relaxation time is defined as when the distance between the steady-state attractor and the state in the logarithm-converted phase space first becomes less than 0.05.

For visualizing the differences among the trajectories, we analyzed all the trajectories in the phase space by the principal component analysis (PCA, see Sec. II), where all the trajectories are converted to the logarithmic scale. We plotted all trajectories projected onto the 2-dimensional principal component space (PCS) in Fig. 2(d). The trajectories were

classified into two groups by the relaxation time and differently colored. The first group is quickly-relaxing trajectories that the trajectory in the top panel of Fig. 2(a) belongs to (colored in green-white-purple). The trajectory in the bottom panel of Fig. 2(a) is grouped into the other group, colored blue-white-red, which takes much longer to relax to the steady-state attractor.

The remarkable gaps between the timescale of chemical reactions and, accordingly, the growth rate during their relaxations highlight the difference between the two time courses. The specific growth rate μ at the steady state is ≈ 0.5 hour^{-1}, and the model cell achieves this growth rate in a few seconds in the top panel of Fig. 2(a), while less than 10^{-10} hour^{-1} in the bottom panel at $t = 10^2$ hours (at plateau). Thus, in the following sections, we call the trajectories of the second group "dormant trajectories" because of their much slower growth rate than the other group. Accordingly, the trajectories of the first group are termed "growth trajectories". The following
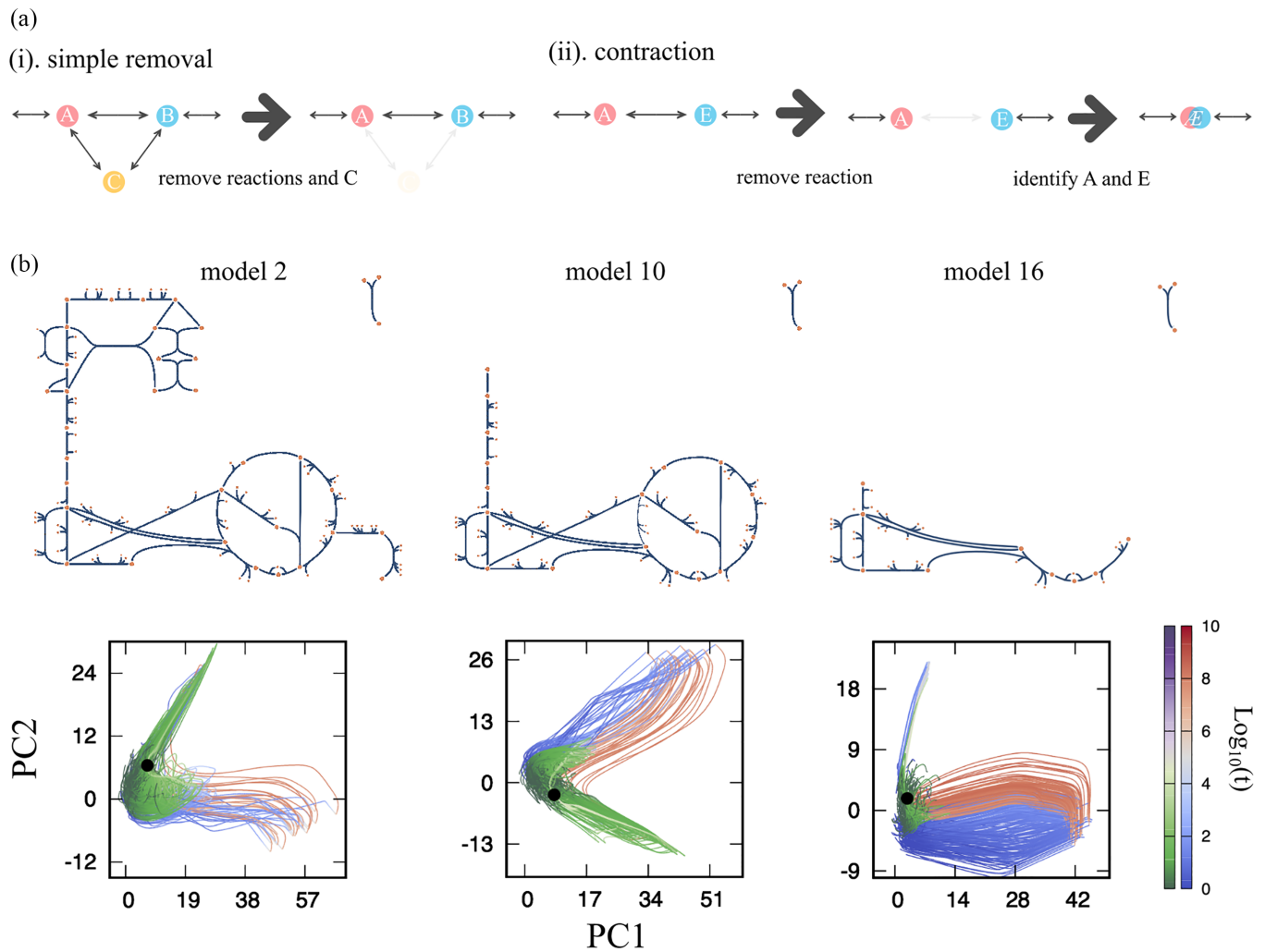
FIG. 3. (a) Two types of reaction removal. The simple removal removes one or a few reactions from the network. The number of reactions to be removed is determined so that the removal does not make the dead-end chemicals. The contraction removes a single reaction first, and then, the substrate and product of the removed reaction are identified and regarded as a new chemical species. (b) The reduced networks of the intermediate models (models 2, 10, and 16) are drawn. The only nutrient (glucose) is at the top left corner of the network. The trajectories projected onto the PCS of each model are also shown. For the coloring protocol of the trajectories, see the main text.

sections are devoted to unveiling the mechanism leading to the differentiation of the growth and dormant trajectories.

C. Systematic model reduction

In the previous section, we saw that distinct relaxation dynamics emerge depending on the initial concentrations of the metabolites. Interestingly, we found that the emergence of distinct dynamics is a robust feature of the *E. coli* core model. The distinct dynamics emerge even if we use the mass-action kinetics instead of the Michaelis-Menten function for the reaction-rate function. Also, it is less sensitive to the specific choice of the parameter values (see Appendices B and H). This robustness implies that the distinct dynamics emerge from the structure of the metabolic reaction network of the *E. coli* core model rather than choices of specific parameter values.

Thus, it is worth asking if there are understandably simple, minimal network architecture(s) in the *E. coli* core network which lead to the distinct trajectories. In the present section,

we reduce the *E. coli* core network to obtain a minimal network exhibiting distinct relaxation dynamics. As far as we know, there is no method to reduce the reaction network without losing the characteristic nature of the relaxation dynamics. Once the concentrations of the cofactors are dealt with as variables, metabolic reactions in the model get highly interconnected, and the well-known reduction method works poorly. For instance, adiabatic elimination may eliminate merely one or few reactions, and obtaining an understandably simple model is hopeless. Thus, here we focus only on the emergence of distinct trajectories. As will be seen, this allows us to derive a much simpler model than the original model.

In the following, we remove one or a few reactions from the network step by step and check if the reduced model still exhibits distinct trajectories (a solid criterion is introduced later). As illustrated in Fig. 3(a), we consider two types of reaction removal, namely, simple removal and contraction. First, we describe the simple removal. Suppose that there are reactions $A \rightleftharpoons B$, $B \rightleftharpoons C$ and $C \rightleftharpoons A$, and also A and B are connected to the rest part of the network by the other reactions [Fig. 3(a)(i)].

The simple removal removes the reaction $B \rightleftharpoons C$ and $C \rightleftharpoons A$, and, accordingly, eliminates the chemical C because it is a disconnected component in the network.

In contrast, chemical species are merged by the contraction [Fig. 3(a)(ii)]. It removes a reaction $A \rightleftharpoons E$, and then, the chemical A and E are identified, forming a new chemical Æ. Here, we avoided the appearance of the dead-end chemical, which has only one reaction because networks with dead-end chemicals can cause a heavy accumulation of the chemicals, potentially leading to an artifactual anomalous relaxation behavior.

At each reduction step, we checked if the reduced model exhibits the two distinct classes of trajectories by computing its dynamics (For the details and the criterion for the distinct dynamics, see Appendix C). In the following we use the model with the mass-action kinetics with most parameters to be unity because we have confirmed the distinct dynamics also emerge with this setup (for the detailed setups, see Appendix B).

We have reduced the *E. coli* core model step-by-step according to the model reduction method described above (The pseudo-code is presented in Algorithm 1 in Appendices). For accomplishing the network reduction, we manually determined the order of the reaction removal so that subsystems of the network are removed or contracted in consecutive reduction steps. We completed the model reduction by removing and contracting the L-glutamine synthesis pathway (4 steps), pentose-phosphate pathway (4 steps), glycolytic pathway (3 steps), and TCA cycle (7 steps) with the indicated number of steps in the parenthesis. The full list of the removed reactions is provided in *SI Data*.1 within the Supplemental Material [42]. Note that we also tried the model reduction in random orders of the reaction removal (see Appendix G). The minimal networks led by the reduction surely depend on the order of the reaction removal. However, all the minimal networks commonly satisfied the two conditions for the emergence of the distinct trajectories discussed later. We revisit the case of random-order reduction in Sec. IV.

The reaction network, and the trajectories projected onto the PCS of selected models are shown in Fig. 3(c). We colored the trajectories based on the relaxation time of each. The figure shows that dormant trajectories (blue-white-red trajectories) commonly take detours to reach the attractor in the PCS. We confirmed that the dormant trajectory also takes detours in the original high-dimensional phase space (Appendix C 5).

D. A minimal model

After the 18 steps of reductions, we reached the stage where no more reduction is possible without losing the distinct dynamics. The reaction network and names that remained in this minimal network (model 18) are depicted together with the original *E. coli* core network in Fig. 4(a). The network consists of glucose (glc), phosphoenolpyruvate (pep), pyruvate (pyr), oxaloacetate (oaa), ATP, ADP, and AMP. As highlighted in the original network, the reaction from glc to pep is the contraction of the glycolytic pathway, and oaa is representative of the chemicals in the TCA cycle. It is worth noting that the network's local structure among pep, pyr, and oaa is unchanged (cyan boxes). In other words, the minimal network

is obtained by removing the pentose phosphate pathway and contracting the glycolytic pathway and the TCA cycle. Also, the reaction ADK1 converting two ADPs to ATP and AMP is conserved. As shown in Figs. 4(b) and 4(c), the model still exhibits distinct trajectories. In the following, we use one-letter variables instead of the abbreviations of the metabolites. x, y, z and g denote [pep], [pyr], [oaa], and [glc], respectively. a, b, and c are assigned for [atp], [adp], and [amp], respectively. We use the upper-case characters for referring to the name of the metabolites (i.e., X indicates phosphoenolpyruvate, and x means its concentration [pep]).

The model consists of five variables (recall that g and $a + b + c$ are constant). We wish to simplify the model further and draw the two-dimensional vector field. Thus, we tried the adiabatic elimination of the concentrations of three chemicals (because now we have the five variables). By checking all the possible combinations of three chemicals, we found that the adiabatic elimination of a, b, and z does not lose the distinct dynamics. The set of ODEs of the minimal model is then given by

$$\frac{dx}{dt} = -(ax - bg) - (x - \kappa z) + (ay - \kappa cx)$$
$$- (bx - \kappa ay) - (d + rza)x, \quad (2)$$

$$\frac{dy}{dt} = -(ay - \kappa cx) + (bx - \kappa ay) - (d + rza)y, \quad (3)$$

where a, b (accordingly $c = A_t - a - b$ with A_t as the total concentration of adenosine energy carriers), and z are adiabatically solved, and thus, are the functions of x and y.

The two-variable system allows us to visualize the vector field. As shown in Fig. 4(d), interestingly, there is a boundary below and above which the streamlines change the direction dramatically ($x \lesssim 0.1$ and $y \approx 1$). Below the boundary, the state relaxes to the attractor rather straightforwardly, corresponding to the dynamics shown in Fig. 4(b) (growth trajectory). On the other hand, trajectories starting from the upper region first travel to the left side of the phase space (small x region) and return to the attractor, corresponding to Fig. 4(c) (dormant trajectory). We attribute the emergence of the distinct trajectories to this dramatic change in the direction of the vector field across the boundary. Hereafter, we call the region above- and below the boundary the dormant and the growth region, respectively.

E. Conditions for the emergence of distinct trajectories

What determines the boundary between the growth- and the dormant region, and why is the vector field of the two-variable model [Fig. 4(d)] almost parallel to the horizontal axis in the dormant region? For the first point, we found a large gap between the two regions in a and b. In the dormant region, their concentrations are low ($\sim 10^{-8}$), while in the growth region, they are in the order of 0.1. This gap gives an insight into the second point. We found that the drastic change in the direction of the vector field occurs because four of the five reactions of the model coupled with the adenine nucleotide carriers. Thus, these reactions halt almost entirely in the dormant region.
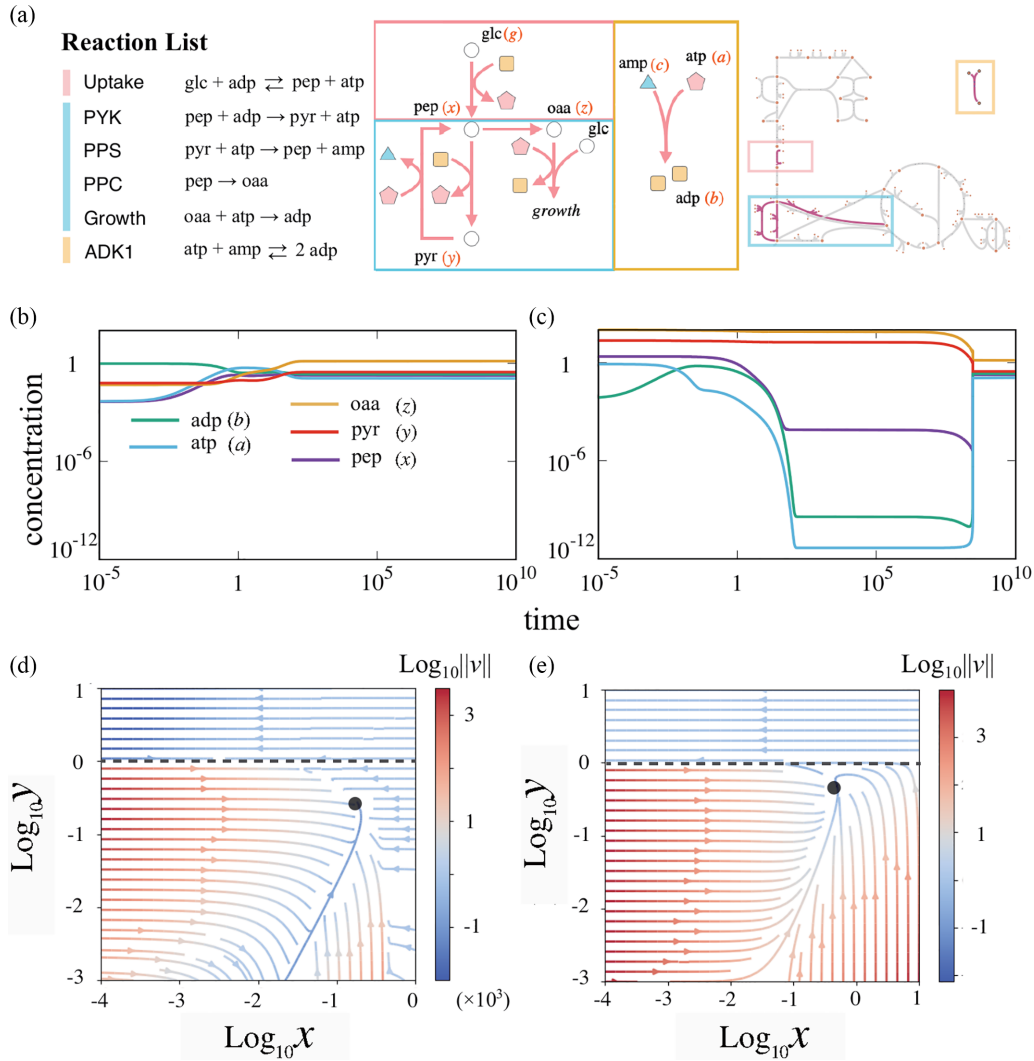
FIG. 4. (a) The list of the reactions in the minimal network (left). The structure of the minimal network (middle). The original network with the reactions in the minimal model is highlighted (right). The minimal model consists of three parts, namely, the glycolytic pathway (pink bar and boxes), the joint part between the glycolytic pathway and the TCA cycle (cyan bar and boxes), and the adenosine kinase reaction (yellow bar and boxes). [(b), (c)] Example time courses of the growth trajectory (b) and the dormant trajectory (c) of the minimal model. (d) The streamline representation of the vector field of the two-variable minimal model where the steady values of [atp], [adp] and [oaa] under given [pep] and [pyr] are numerically solved. (e) The streamline representation of the simplified minimal model. The color indicates the norm of the vector $v = (dx/dt, d[pyr]/dt)$ at each point, and the black dots indicate the attractor of each in (d) and (e). $\phi_0 = 10^{-8}$ in (e). The dashed lines in (d) and (e) represent the boundary where the direction of the vector field changes dramatically ($y = 1$). The lines are drawn according to the Eq. (4) for (d) and the definition of ϕ for (e).

Intuitively, the low values of a and b in the dormant region can be understood from the reactions in Fig. 4(a) as follows. First, let us consider the situation where x and y are in the dormant region. If, in addition, x is low, the uptake reaction proceeds in the direction $G + B \rightarrow X + A$. When this reaction accumulates some ATP, PPS proceeds in the direction $Y + A \rightarrow X + C$, because x is low. In total, the uptake reaction and PPS form a futile cycle that converts A and B into C. Note that the PPS does not easily result in the accumulation of X, because of PPC reaction. If x is high, but y is also high so that the system is still in the dormant region, PYK plays the same role as the uptake reaction in the previous case. Thus, a futile cycle converting A and B into C is formed in both cases. If the conversion from A and B into C is slow enough, the other reaction, ADK1 ($A + C \rightleftharpoons 2B$) proceeds to balance $A + B$ and

C. However, ADK1 cannot balance them if the conversion is too fast because the reaction needs A.

Indeed, this intuitive description is consistent with the analytical estimate of the boundary. We derive the boundary between the growth and dormant region for $x \ll 1$. The boundary is given by y leading to a low a and b with a given value of x. For the estimation of the critical y, we sum up da/dt and db/dt and assume $a, b, x = O(\epsilon)$ with $\epsilon \ll 1$. Also, recall that the irreversibility parameter κ in [Eq. (2)] is small, and thus, we omit κ term [44]. Then we obtain

$$\frac{d(a+b)}{dt} = J_{ADK1} - J_{PPS} \sim a(v_{ADK1}A_t - v_{PPS}y), \quad (4)$$

where we explicitly write down the rate parameter v_*'s for the interpretation of the estimate. If the first term of the rightmost

side is larger than the second term, $a + b$ increases, while in the opposite situation, the sum keeps decreasing to zero as long as a is nonzero. This shift occurs at $v_{PPS}y \sim v_{ADK1}A_t$, and it gives the boundary between the growing and the dormant regions.

Next, we explain how the decrease of a and b leads to the vector field parallel to the horizontal axis in the dormant region [Fig. 4(d)]. Let us assume that a and b are approximately the same and well-represented by a single lumped parameter ϕ. Also, we set the irreversibility parameter κ to zero for simplicity. Then, the ODE for the two-variable minimal model [Eq. (2)] is given by

$$\frac{dx}{dt} = \phi(1 - x + y + rz) - (1 + d)x, \tag{5}$$

$$\frac{dy}{dt} = \phi(x - y + rz) - dy, \tag{6}$$

where z is the function of ϕ, while it becomes constant as ϕ approaches 0. From the equation, we can see that if a and b, represented by ϕ, are $O(1)$ (i.e., in the growth region), the timescale of the system is $O(1)$. On the other hand, if A and B deplete and $\phi \approx 0$ holds in the dormant region, the timescale of dy/dt becomes $O(d)$. Since the spontaneous degradation rate d is sufficiently smaller than unity, $|dx/dt| \gg |dy/dt|$ holds, and it leads to the vector field being almost parallel to the x axis as depicted in Fig. 4(d).

To confirm if the simplification above still captures the feature of the vector filed in Fig. 4(d), we have drawn the vector field of the simplified model Eqs. (5) and (6) with $\phi = \max\{1 - y, \phi_0\}$ in Fig. 4(e). It well captures the feature of the original vector field. We have confirmed that the shape of the vector field is robust to the choice of the function ϕ. Also, we analytically solved the model without the growth dilution term [Eqs. (5) and (6) with $r = 0$] and found that the model has only a single timescale which is $O(1)$ in the growth region (see Sec. D).

The simplified model [Eqs. (5) and (6)] highlights that the timescale of dx/dt is much faster than that of dy/dt in the dormant region. The right hand side of Eq. (5) has the term $(1 + d)x$, while that in Eq. (6) is only the degradation term dy, and this difference results in the parallel streamline in the phase space [Fig. 4(e)]. It is worth noting where the term $(1 + d)x$ in Eq. (5) comes from. d corresponds to the constant-rate degradation term, and the reactions coupled with either A or B should have the rate proportional to ϕ. Therefore, this timescale 1 comes from the reaction coupled neither with A nor B, namely, PPC ($X \to Z$). All the reactions except PPC are coupled with either A or B, and thus, the reactions slow down over the boundary between the growth- and the dormant region. However, the rate of PPC has no direct effect from the depletion of A and B. Then, even after the slowing down of almost all reactions, X is kept being consumed, and it leads to the characteristic dynamics of the dormant trajectory.

Note that, if PPC were also coupled with A and B, $(1 + d)x$ term in Eq. (5) would have been replaced by $(\phi + d)x$. In such a case, all the reactions would have been uniformly slowed down by the depletion of A and B, and the direction of the vector field would not change over the boundary as drastically as Fig. 4(d). Thus, it is vital that the reaction system partially slows down due to the depletion of A and B.

It is noteworthy that the network structure is also a part of the mechanism: If PPC were the reaction converting Y to Z instead of X to Z, the drastic change of the direction of the vector field as Fig. 4(d) would not result. If PPC were $Y \to Z$, the main body of the reaction network (reactions except for ADK1) would have no branch. The slowing down of the upstream reactions of PPC (i.e., uptake, PYK, and PPS) would be rate-limiting steps of it, and PPC would slow down coordinated with these reactions.

The above two points suggest that large discrepancies in the chemical concentrations between the steady state and the plateaux lead to distinct dynamics. In both cases—PPC with energy coupling and the main network without a branch—the reactions uniformly slow down. In such scenarios, even if A and B deplete, the difference between the production and consumption of each chemical stays relatively small. Thus, the changes in the concentrations remain small. However, if the slowing-down occurs heterogeneously on the network, some chemicals will have a significant mismatch between production and consumption. As a consequence, the concentrations of such chemicals drastically change from the concentrations before the depletion of A and B.

To sum up, the mechanism of the emergence of the distinct trajectories has two parts: (i) the unbalance of energy (ATP and ADP) production and consumption, and (ii) partial slowing down of the reaction system caused by nonuniform coupling to the energy currencies and branching of the network.

IV. DISCUSSION

We have shown that *E. coli* central carbon metabolism exhibits distinctly different dynamics depending on the perturbation from the steady-state concentration. The two types of trajectories greatly differed in terms of the relaxation time and the growth rate during the relaxation, and thus, we termed them as the growth- and the dormant trajectories. We systematically reduce the reaction network without losing the distinct trajectories. By the successive reduction of the model, we eventually reached the minimal network still exhibiting the qualitatively same behavior.

By drawing the vector field of the two-variable minimal model, we found that there is a boundary at which the vector field changes the direction drastically. Indeed, the two regions are divided by the boundary corresponding to the set of the initial points of the growth- and the dormant trajectories. The analysis led that there are at least two vital requirements for the distinct trajectories: (i) the unbalance of the energy production and consumption and (ii) the partial slowing-down of the reactions due to the nonuniform coupling with the energy currency molecules and branching of the network.

By studying several model variants, we carefully examined the robustness of our main results, namely, the emergence of distinct trajectories and the consequence of model reduction. First, the robustness of the emergence of distinct trajectories to the parameter values was examined. For several values of the total adenine nucleotide carriers concentration (A_t), we randomly assigned the rate constants and studied if the distinct trajectories still emerged. As anticipated from the analysis, the distinct trajectories robustly emerge as long as the total

concentration of adenine carriers A_t is not too large for the depletion of ATP and ADP to occur (see Appendix H). As well as the random parameter values, we performed the reaction removal for the model reduction in 16 different randomized orders. All the minimal networks obtained by the random reduction were larger than those derived in the result section but shared the main features argued above, namely, (a) the models keep ADK1 reaction and AMP, and (b) in each network, there are both reactions, with and without the coupling to the energy currency molecules (ATP, ADP, and AMP) as well as branches.

We checked the outcomes of relaxing the assumptions that we made initially. It is confirmed that the model without the replacement of the nicotinamide nucleotide carriers by the adenine nucleotide carriers exhibits distinct trajectories (Appendix F). Also, we have confirmed that the distinct trajectories emerge if the assumption on the constant total concentration of the adenine nucleotide carriers is relaxed by introducing a phenomenological reaction for the *de novo* synthesis of AMP to the minimal model (Appendix E). Overall, the emergence of distinct trajectories is a robust feature of the *E. coli* core model rather than a phenomenon led by fine tuning of the parameters.

Two transition paths to the dormancy were schematically proposed by M. Heinemann's group [11,13]. The first path is the transition triggered by stochastic gene expression. For example, the elevated concentration of the toxin protein inhibits several cellular processes and leads to the ppGpp-mediated stress responses [45,46]. There are multiple mathematical models in accordance with this "genetically-triggered" scenario [14,47–51]. The second path is "metabolically-triggered". The disturbance of the metabolic state induces the stress response to modulate the gene expression pattern. While the disturbance of the metabolic state is attributed to the stochastic fluctuations of the enzyme level in the papers [11,13], the distinct dynamics due to the nonlinearity of the metabolic reactions should be able to play a role in the transition.

The present model showed a possibility that the dormancy transition could be triggered by the metabolic dynamics itself when the metabolic state is perturbed. According to the minimal model, the perturbation evokes a futile cycle and leads to the depletion of ATP and ADP. Here, the sources of the perturbation can be starvation, nutrient shift, exposure to antibiotics, pH stress, or even stochasticity of the intracellular processes.

However, in reality, the intracellular states of the dormant cells may go beyond what we can depict in terms of metabolites. We did not consider a dynamic change in enzyme concentrations in the current model analysis, which would modify chemical reaction rates. While a constant enzyme concentration assumption is plausible in steady-state growth, gene regulations of enzyme levels are likely to be relevant in dynamically changing growth processes. Indeed, disruptions of the metabolic states may lead to several responses, such as the stress-response systems controlled by (p)ppGpp, toxin-antitoxin modules, and/or the alternative sigma factor σ^S [11,52–57]. Since the response systems work to relieve the disruption of the metabolic state, such a strong drop of the concentrations of the metabolites found in the present study may be avoided by gene regulation of relevant enzymes.

While further research on the effect of the gene-regulation dynamics is needed, we believe that the present findings provide a possible mechanism to trigger dormancy where the disruption of the metabolic state may lead to even bigger responses.

Note that we can find the counterpart of the reactions in the minimal model in the full *E.coli* metabolic network. Thus, the dormancy transition demonstrated by the minimal model is verifiable by experiments. The central part of the mechanism is that PPS and PYK can form a futile cycle and the competition between PPS and ADK1 on the consumption/production of ATP. Indeed, the experiments showed that one could induce the ATP-consuming futile cycle between phosphoenolpyruvate and pyruvate via PYK and PPS by overexpressing the ppsA gene [58,59]. Taking the experimental reports and the present computational results together, we hypothesize that the overexpression of the pps gene leads to an increase in the persister fraction because PPS converts ATP to AMP.

Lastly, we like to remark that the requirements for the metabolic network to show the distinct trajectories are not limited only on the *E. coli* core model. We can find several reactions that potentially form a futile cycle from various species. For instance, each of acetyl-CoA synthetase (KEGGID:R00235), phosphoribosylpyrophosphate synthetase (R01049), and asparagine synthase (R00578) [60] converts ATP to AMP and forms a loop in the metabolic networks. These are the minimum requirements for a reaction to form a futile cycle discussed above. Such reactions are widespread from prokaryotes to eukaryotes and from unicellular to multicellular organisms. Comprehensive studies of the kinetic models of not only *E. coli* but also other organisms may pave the way for understanding the robust and generic network features leading to the multiple timescales of cellular growth and dormancy.

APPENDIX A: THE *E. COLI* CORE MODEL WITH BIOLOGICALLY REALISTIC PARAMETER VALUES

It is worth asking if the model exhibits distinct trajectories with biologically realistic kinetic values. However, obtaining the kinetic parameters for all reactions, even in a rather small *E. coli* core model, is still challenging. Thus, we take advantage of the metabolic ensemble modeling (MEM) [31,33], which is a method for the parameter estimation of the metabolic models. In the MEM approach, each enzymatic reaction is decomposed into a sequence of elementary reactions, i.e., an enzymatic reaction $A + B \rightleftharpoons C$ catalyzed by E is, for instance, decomposed as follows:

$$A + E \rightleftharpoons AE, \tag{A1}$$

$$AE + B \rightleftharpoons ABE, \tag{A2}$$

$$ABE \rightleftharpoons CE, \tag{A3}$$

$$CE \rightleftharpoons C + E. \tag{A4}$$

Note that the rates of elementary reactions [Eqs. (A1)–(A4)] can be represented by the mass-action kinetics. For example, the forward reaction of Eq. (A1) is given by

$$v_{A+E \to AE} = k_{A+E \to AE}[A][E],$$

where $k_{A+E \to AE}$, $[A]$, and $[E]$ represents the rate constant of the reaction $A + E \to AE$, the concentration of the chemical A, and the concentration of the free enzyme E (E not in the complex form). Let $[A]_{ss}$ and $[E]_0$ be the steady-state concentration of the chemical A and the total concentration of the enzyme E, respectively. Then at the steady state, the logarithm of the reaction flux is

$$\ln v_{A+E \to AE} = \ln(k_{A+E \to AE}[A]_{ss}[E]_0) + \ln([E]/[E]_0).$$

Note that the term depending on $[A]$ is dropped because $\ln[A]/[A]_{ss}$ is zero at the steady state. The MEM approach seeks the values of the scaled rate constant such as $\tilde{k}_{A+E \to AE} = k_{A+E \to AE}[A]_{ss}[E]_0$ and $e = [E]/[E]_0$ so that the model can fit the experimentally obtained fluxome data using the ensemble modeling [61]. (for more detail, see [31,33])

For the simulation of the *E. coli* core model, we adopted the parameter values estimated by Khodayari *et al.* [33]. For obtaining the values of (nonscaled) rate constants, we need to divide the scaled rate constants by experimentally reported concentrations of chemicals because what they estimated are, for instance, in the form of $k_{A+E \to AE}[A]_{ss}[E]_0$. We calculated the rate constants by using the concentration data measured by Gerosa *et al.* [62] and estimated by Akbari *et al.* [63]. Since the concentration of glyoxylate was presented in neither [62] nor [63], we used the geometric mean of the concentrations of two neighbor metabolites in the metabolic network, isocitrate and L-malate. The back-calculated parameters are presented in *SI Data*.2 within the Supplemental Material [42]. After the back-calculation of the rate constants, we constructed an ODE model. We adiabatically eliminated the elementary reactions for each enzymatic reaction in the model and used the Michaelis-Menten type rate equation (see [33]).

In growth dynamics [Fig. 2(a) in the main text], the concentration of a chemical species, glutamine, becomes lower than 1 nM. Glutamine is one of the growth factors in the current setup. We attribute this extreme drop to the following technical reason: In contrast to the present model, the biomass synthesis reaction was not incorporated into the model in [33] where the kinetic parameters were estimated. Therefore, glutamine is consumed much faster in the present model than in the model used to estimate the parameters.

APPENDIX B: SIMPLIFIED MODEL WITH MASS-ACTION KINETICS

The kinetic *E. coli* core model is, as it is, too complicated to understand the mechanism that leads to the two distinct relaxation trajectories. Thus, we simplified the *E. coli* core model as follows. First, we modified the kinetics of the chemical reactions from the Michaelis-Menten formula to the mass-action

rate equation. The rate of the ith chemical reaction $A \rightleftharpoons B$, J_i, which was given by

$$J_i = v_i \frac{[A] - k_i[B]}{1 + [A]/K_A^{(i)} + [B]/K_B^{(i)}} \tag{B1}$$

is replaced by

$$J_i = v_i([A] - k_i[B]), \tag{B2}$$

where v_i and $v_i k_i$ are the forward and backward reaction rate constant, respectively. Note that the mass-action kinetics [Eq. (B2)] is a special form of the Michaelis-Menten kinetics [Eq. (B1)] in the parameter region where $[A] \ll K_A^{(i)}$ and $[B] \ll K_B^{(i)}$ hold (for general arguments, see [64]). The model is then nondimensionalized by scaling the concentrations by the external glucose concentration and the time by the rate constant of the glucose uptake. We further simplified the rate equations by setting v_i's to unity and binarising k_i's for all i's. The *E. coli* core model contains the information of irreversibility for each reaction, and thus, if the ith reaction is reversible, we set k_i as unity, and otherwise, set it to $\kappa \ll 1$. We term this simplified version of the kinetic *E. coli* core model as model0 with an index for the following model reduction steps.

Surprisingly, the emergence of distinct relaxation trajectories is robust to such an extensive model modification. The qualitative difference of the trajectories [Fig. 5(a)], bimodality of the distribution of the relaxation time [Fig. 5(b)], and the distinction of the trajectories in the PC1-PC2 space [Fig. 5(c)] were unchanged. This robustness implies that the emergence of the distinct trajectories stems from the structure of the metabolic reaction network of the *E. coli* core model rather than choices of specific parameter values. We also confirmed that the distinct trajectories emerge if the kinetic parameters are randomly assigned instead of setting them to unity (see Appendix H).

APPENDIX C: MODEL REDUCTION

1. Criterion for distinct trajectories

For each model reduction step, we run the ODE model from 512 randomly generated initial points to search the attractors. Except for a single model, all the intermediate models of the reduction process showed monostability (see Appendix C 6). Then, 512 initial conditions were generated by perturbing the steady-state concentration in the same way as we did in the previous models.

The bimodality of the relaxation time distribution is one of the best intuitive criteria for distinct trajectories. However, we found in some cases, the bimodality was unclear even though there were clearly different types of trajectories when we plotted the time courses and performed PCA. This is because the growth rates during the relaxation of both types of trajectories (growth and dormant) become smaller than the spontaneous degradation rate d. Thus, the relaxation time of all the trajectories becomes approximately $1/d$. It is possible to overcome this problem by setting d to be sufficiently small such as 10^{-20} in principle, but the computation time becomes unbearably long. Thus, we decided to focus on the similarity of the trajectories instead of the relaxation time itself. For interested readers, the distributions of the relaxation
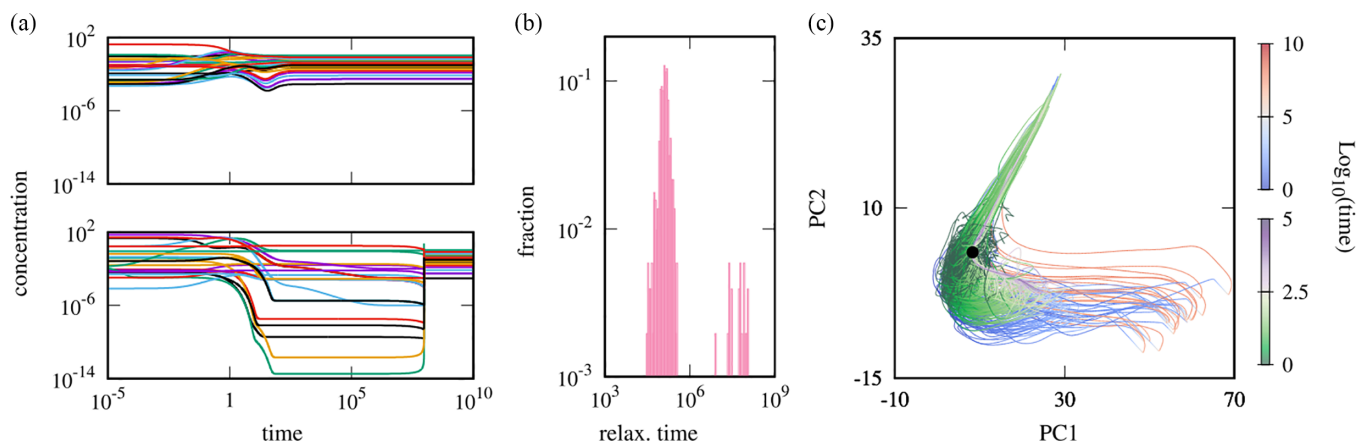
FIG. 5. (a) Two characteristic dynamics of the model 0 starting from different initial points. The relaxation behaviors are qualitatively different between the top and bottom panels. (b) The distribution of the relaxation time showing a clear bimodality. (c) Trajectories are overlaid in two-dimensional principal component space. The color indicates $\log_{10}$ of time. The trajectories having shorter relaxation time [top panel of (a)] are colored green-white-purple while the others are colored blue-white-red. The black point corresponds to the attractor. Initial concentration of each metabolites is $10^{u_{i,n}}[X_i^{(ss)}]$ with $[X_i^{(ss)}]$ as the steady-state concentration of the ith metabolite, and $u_{i,n}$ as a random number uniformly distributed in $[-2, 2]$ while the total concentrations of adenine nucleotide carriers are normalized. $v = 1$ and $\kappa = 10^{-6}$ for all reactions. Other parameters are $[\text{glc}] = 1$, $A_t = 1$, $r = 0.1$, and $d = 10^{-8}$.

time for all the models in the reduction step are presented in Appendix C 3.

Below, we first intuitively explain how we quantify the similarity of the trajectories and then introduce the actual measure.

Suppose that a model has a single attractor. Then, all the trajectories starting from different initial points eventually converge. We like to categorize the trajectories into different groups so that if a pair of trajectories monotonically approach each other as they converge to the attractor, they belong to the same group. One may naïvely expect that we can state that two trajectories $x(t)$ and $y(t)$ monotonically approach each other if the Euclidean distance between them at the same time point $d(x(t), y(t))$ is a monotonically decreasing function of t. However, since the initial points are distributed in the phase space, measuring the distance between the points on two trajectories at the same time point is unreasonable.

Thus, instead of adopting this naïve definition of monotonicity, we measure the maximum Euclidean distance between two trajectories in the phase space. It is known as the Hausdorff distance of the trajectories, given by

$$d_H(x, y) = \max\{\max_t \min_s d(x(t), y(s)), \max_t \\ \times \min_s d(x(s), y(t))\}. \quad (C1)$$

The Hausdorff distance first looks for the closest point of trajectory y from the point $x(t)$, $y(s^*(t))$, and then find the pair of the points $(x(t), y(s^*(t)))$, which gives the maximum Euclidean distance. The same is done from the points of $y(t)$ and the larger value is chosen for the symmetry $d_H(x, y) = d_H(y, x)$. The Hausdorff distance thus measures how far the two trajectories are distant while trivially distant pairs of points are not taken into account (for example, the initial point of x and the endpoint of y, i.e., the attractor).

We cannot judge whether the trajectories go away from each other or not directly from the Hausdorff distance since

it needs to be compared with the initial separation. Thus, we normalize the Hausdorff distance by the Euclidean distance between the initial points, $d(x(0), y(0))$ leading to

$$R(x, y) = \frac{d_H(x, y)}{d(x(0), y(0))}. \quad (C2)$$

We call this ratio $R(x, y)$ as the expansion ratio of the trajectories x and y. It measures how much the initial distance has expanded. If $d_H(x, y)$ is smaller than the initial distance, $R(x, y)$ is less than unity. $R(x, y) > 1$ means that two trajectories go away from each other at least once despite eventually converging to the same attractor. Note that in this paper, the Euclidean distance, and accordingly, the Hausdorff distance are measured in the original high-dimensional phase space after applying the logarithm-conversion of the variables, not in the lower-dimensional principal component space.

The distribution is expected to have a trivial peak around $R = 1$. If the distribution has only a trivial peak, it indicates that all the trajectories are monotonically attracted to a single predominant stream in the phase space reaching the attractor. Oppositely, suppose the distribution has a nontrivial peak(s) and/or an additional long tail. In that case, the correlation between the initial distance and the Hausdorff distance is not simply scaled to each other.

Therefore, in the present paper, we utilize the multimodality and/or the long tail of the distribution of the expansion ratio as the criterion of the distinct trajectories (examples can be found in Appendix C 3). We examine if the model has exhibited distinct trajectories by fitting the distribution by a sum of Gaussian functions. In rough terms, it checks if the distribution needs at least two Gaussian functions with distant peaks (see Appendix C 2 for the details). Note that in the following analysis, the computation of the expansion ratio and PCA were performed for the trajectories converted to the logarithmic scale so that the dynamic behaviours of the chemicals with low concentrations are also reflected in the analysis (As a side effect of the logarithm conversion,
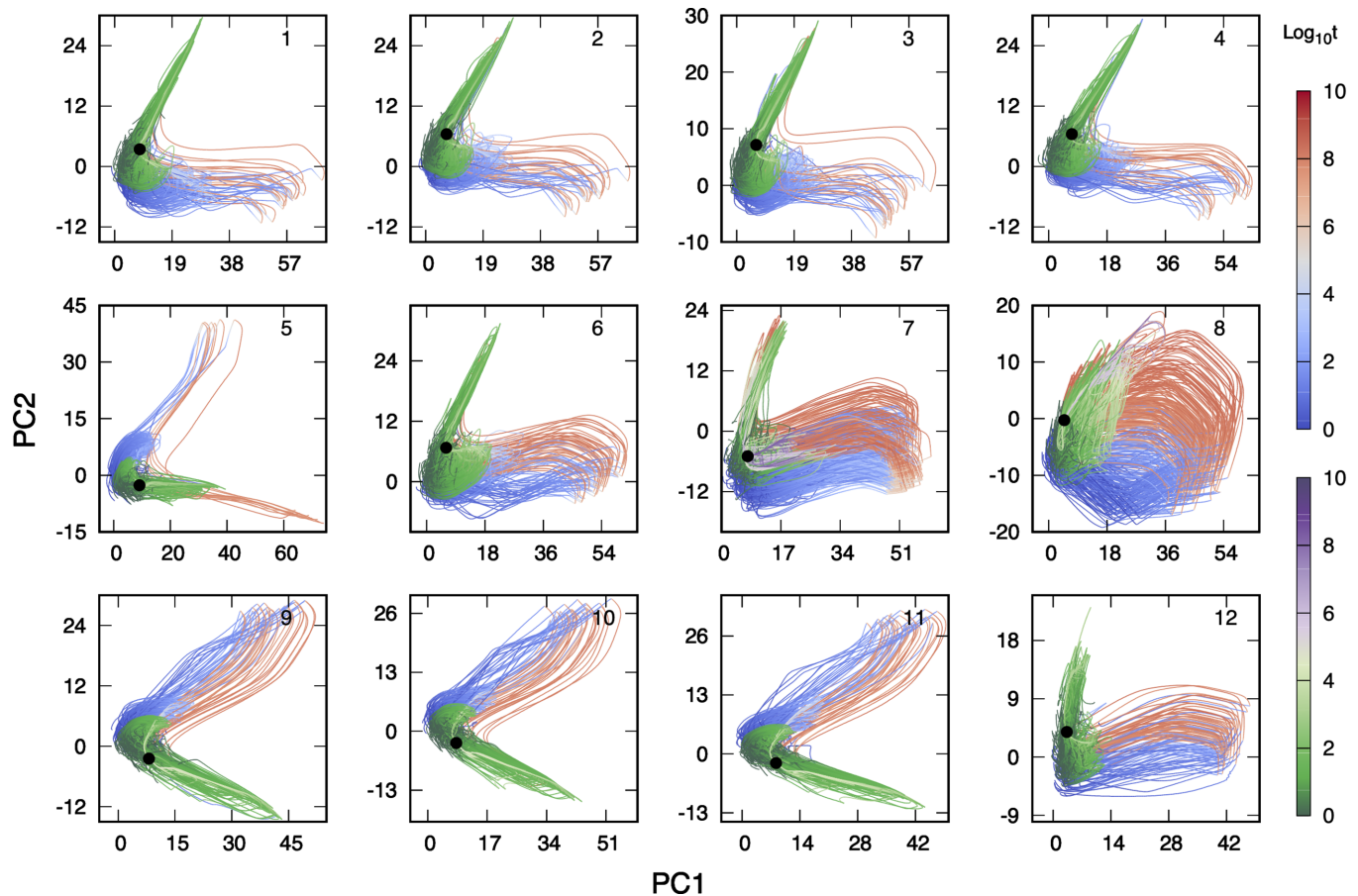
FIG. 6. The trajectories on the PCS (from model 1 to model 12).

the behaviors of the chemicals with quite low concentrations may be too much highlighted. We computed the expansion ratio with cut-offs of the concentrations for a lower side, see Appendix C 4).

2. Judging multimodality

Let us suppose that there is a list of the expansion ratio $\{R(x, y)\}_{x,y \in \mathcal{T}_i}$ where $\mathcal{T}_i$ is the set of the trajectories of the ith model. Then, we fit the histogram of the expansion ratio by a sum of the normal distributions $\mathcal{G}(R, \vec{\mu}, \vec{\sigma}) = \sum_{i=0}^{M-1} w_i \mathcal{N}(R; \mu_i, \sigma_i), \sum_{i=0}^{M-1} w_i = 1, w_i \geqslant 0$ where $\mathcal{N}(R; \mu_i, \sigma_i)$ is the normal distribution with μ_i and σ_i as the mean and the standard deviation, respectively. Here, we heuristically choose M as 4 because the distributions of the expansion ratio often had a heavy tail, and fitting with a small M could prioritize to fit the tail rather than the second peak. We used the python package `sklearn.mixture for the fitting.GaussianMixture` [39] with the options as `covariance_type = "full"`, `tol = 10^{-4}`, `n_init = 16`.

After the fitting, we reorganize the indices of the normal distributions so that $\mu_i < \mu_{i+1}$ holds. We judged the distribution is multimodal if the result fulfills the conditions below:

(i) $\mu_0 < 1.05$ (there is a trivial peak)

(ii) $w_0 \geqslant w_i$ (the trivial peak has the largest weight)

(iii) $1 \leqslant \exists i < M$ s.t., $\mu_i - \mu_0 > \max(1, \sigma_0 + \sigma_i)$ and $w_i/w_0 > 0.01$ (there is another, distant peak)

3. Intermediate models

Here, we present the trajectories on PC1-PC2 space (Figs. 6 and 7), the distribution of the expansion ratio (Fig. 8), and the relaxation time distribution (Fig. 9) for all the intermediate models of the reduction described in the main text. As mentioned in the main text, $d = 10^{-8}$ becomes larger than the growth rate μ at the relaxation plateaux for some models, and in such cases, the relaxation time cannot distinguish the growth and dormant trajectories. According to the importance of $[atp] + [adp]$ that we found in the main text, we wonder if the minimum value of $[atp] + [adp]$ during the relaxation of each trajectory works as a criterion to distinguish the two types of the trajectories. In accordance with the expectation, we found that the distribution of $A_{\min} = \min_{t \in (0,\infty)} \log_{10}([atp](t) + [adp](t))$ of each intermediate model was double peaked. Thus, we colored each trajectory in Figs. 6 and 7 based on which peak of the distribution $A_{\min}$ the trajectory belongs to.

4. The expansion ratio with cutoffs

As shown in Figs. 2(a) and 3(a), the concentrations of some chemicals become too low. Because of the logarithm conversion of the concentrations, these low concentrations can strongly contribute to the multimodal distributions of the expansion ratio to result. To check if the multimodal distribution of the expansion is sensitive to such low concentrations, we
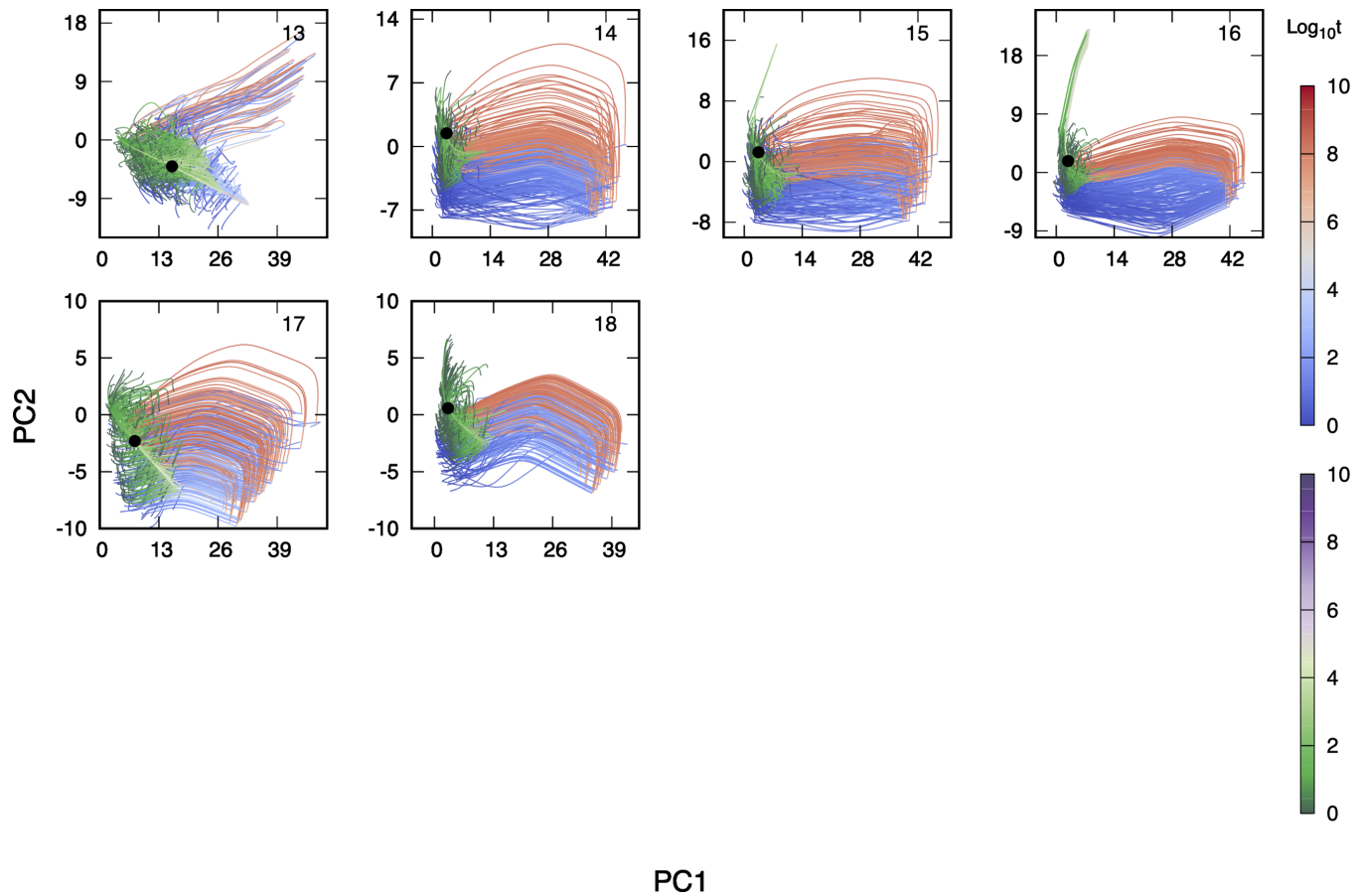
FIG. 7. The trajectories on the PCS (from model 13 to model 18).

computed the expansion ratio of the model 0 with cut-offs. With a given value of cut-off C, we converted each element of the trajectories $\vec{x}(t)$ to $\xi_i(t) = \max(x_i(t), C)$. The trajectories $\vec{\xi}(t)$'s are logarithm converted and then used for computing the expansion ratio. As shown in Fig. 10, the distributions are multimodal up to $C = 10^{-10}$, while the distribution becomes long tailed with two plateaus for $C \gtrsim 10^{-9}$.

5. *L/D* ratio

The trajectories projected onto the two-dimensional PC space give us the impression that the dormant trajectories take roundabout ways comparing the growth trajectories. For the confirmation of the impression, we compare the length of the trajectory in the phase space.

For a trajectory $x(t)$, we introduce two quantities, namely, the line integral of the trajectory $L = \int_x dl$, and the Euclidean distance between the initial point and the attractor $D = d(x(0), x(\infty))$. Since the straight line gives the shortest possible length between two points, the ratio L/D of x measures the deviation of the trajectory x from the shortest path from the initial point to the attractor, representing how far x takes a detour.

For grouping the trajectories, we used the minimum value of $[\mathrm{atp}] + [\mathrm{adp}]$ during the relaxation $A_{\min}$ of each trajectory (see Appendix C 3). We computed the average L/D ratio of the high $A_{\min}$ (growth) and the low $A_{\min}$ (dormant) trajectories,

respectively. As shown in Fig. 11, the average L/D ratio of the low $A_{\min}$ trajectories is larger than that of the trajectories with high $A_{\min}$ values for all the models while the differences are within the error bar in model 5.

6. The minor attractor of model 8

In the model reduction, only model 8 exhibited bistability. The fraction of the initial points relaxing to the major attractor, analyzed in the main text, is approximately 92%.

Here, we apply the same analysis for the trajectories relaxing to the minor attractor to confirm that the choice of the attractor is not crucial for model reduction. We applied perturbation on the minor attractor as $10^{u_{i,n}}[X_i^{(\mathrm{ss})}]$ where $u_{i,n}$ and $[X_i^{(\mathrm{ss})}]$ represents a random number for the ith metabolite and the nth perturbation, uniformly distributed in $[-1, 1]$ and the concentration of the ith metabolite at the minor attractor, respectively.

First, the distribution of the expansion ratio computed from the trajectories relaxing to the minor attractor also exhibited bimodality [Fig. 12(a)]. For the visualization of the trajectories, PCA was performed on the trajectories. In the PC1-PC2 space, the growth trajectories (green-white-purple) and the dormant trajectories (blue-white-red) are clearly separated. Also, the average L/D ratio (see Sec. C 5) with the standard deviation of the growth- and the dormant trajectories are approximately 7.99 ± 3.46 and 9.30 ± 2.44, respectively.
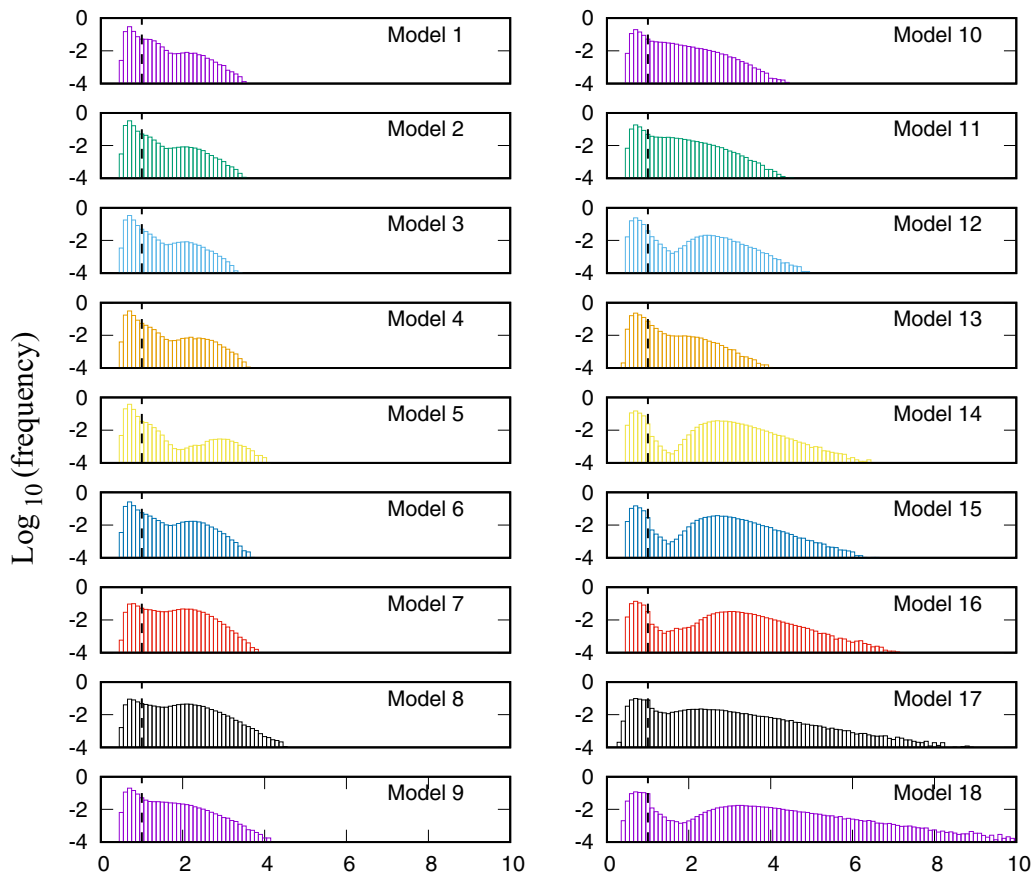
FIG. 8. The distribution of the expansion ratio.

APPENDIX D: ANALYTIC SOLUTION OF THE SIMPLE MODEL AND THE CHOICE OF THE FUNCTION ϕ

For obtaining the analytic solution of the simple model [Eqs. (9) and (10) in the main text] in the growth region, we ignore the growth dilution term here ($r = 0$ case). Then, the ordinary differential equation is given by

$$\frac{d[\text{pep}]}{dt} = \phi([\text{pyr}])(1 - [\text{pep}] + [\text{pyr}]) - (1 + d)[\text{pep}],$$

$$\frac{d[\text{pyr}]}{dt} = \phi([\text{pyr}])([\text{pep}] - [\text{pyr}]) - d[\text{pyr}].$$

We solve this set of equations with

$$\phi = \max\{1 - [\text{pyr}], \phi_0\}. \tag{D1}$$

In the region where $\phi([\text{pyr}]) = \phi_0$ holds, the ODE is linear and, thus, easily solved. In the other region, we transform the variables as $\gamma(t) = [\text{pep}](t) + [\text{pyr}](t)$ and $\delta(t) = [\text{pep}](t) - [\text{pyr}](t)$. Then, temporal evolution of (γ, δ) is ruled by

$$\frac{d\gamma}{dt} = 1 - (1 + d)\gamma.$$

$$\frac{d\delta}{dt} = (1 - (\gamma - \delta)/2)(1 - 2\delta) - (\gamma + \delta)/2 - d\delta.$$

The solution for this is given by

$$\gamma(t) = f^{-1} + C_0 e^{-ft},$$

$$\delta(t) = C_0 e^{-ft} - (\kappa + \eta)/2f,$$

$$+ C_0 \frac{\alpha C_1 U(1+\alpha, 2+\beta; \zeta e^{-ft}) + L_{-(1+\alpha)}^{1+\beta}(\zeta e^{-ft})}{C_1 U(\alpha, 1+\beta; \zeta e^{-ft}) + L_{-\alpha}^{\beta}(\zeta e^{-ft})} e^{-ft}.$$
$$\tag{D2}$$

where U and L are the confluent hypergeometric function and the associated Laguerre polynomial, respectively. Lumped parameters are

$$f = 1 + d,$$
$$\xi(f) = 1 - 3f + f^2,$$
$$\eta(f) = \sqrt{1 - 6f + 3f^2 + 2f^3 + f^4},$$
$$\zeta(f) = \frac{C_0}{f},$$
$$\kappa(f) = -1 + f + f^2,$$
$$\alpha(f) = (\xi(f) + \eta(f))/2f^2,$$
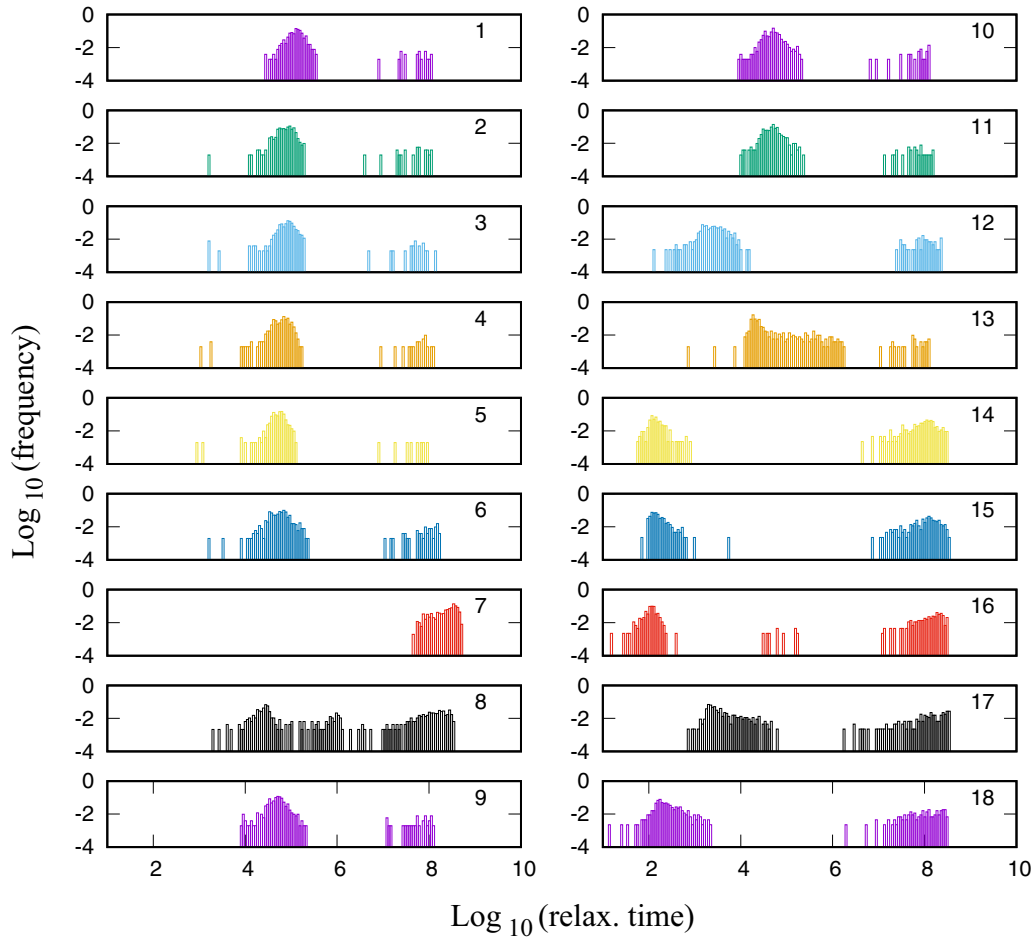$$\beta(f) = \eta(f)/f^2,$$

FIG. 9. The distribution of the relaxation time.

and the integral constants C_0 and C_1 are given by

$$C_0 = \gamma(0) - 1/f,$$

$$C_1 = -\frac{C_0 L_{-(1+\alpha)}^{1+\beta}(C_0/f) + L_{-\alpha}^{\beta}(C_0/f)(C_0 - (\kappa + \eta)/2f - \delta(0))}{C_0 \alpha U(1 + \alpha, 2 + \beta; C_0/f) + U(\alpha, 1 + \beta; C_0/f)(C_0 - (\kappa + \eta)/2f - \delta(0))}.$$

Note that there is only a single timescale $1/f = 1/(1 + d)$ in the growth region. $1/f$ is $\mathcal{O}(1)$ with the default parameter set. While we omitted the growth-dilution term $-\mu[\cdot]$ for obtaining the analytic solution, if the growth rate μ is smaller than 1, the effect of including the dilution term is masked by f. On the other hand, it simply speeds up the relaxation if μ is larger than unity. Thus, the inclusion of μ does not change the argument that the slowest timescale in the growth region is $\mathcal{O}(1)$.

The analytic solution is obtained for a specific functional form of ϕ defined as Eq. (D1). However, the structure of the vector field is not sensitive to the choice of ϕ. In Fig. 13, we drew the two-dimensional vector fields with the functional form of ϕ chosen to be an exponential function $\phi = \exp(-[\text{pyr}])$ (a) and a Hill function $\phi = [\text{pyr}]^{n_H}/(K^{n_H} + [\text{pyr}]^{n_H})$ (b). The figures imply that the nature of the vector

field is robust as long as ϕ reaches a small value as [pyr] increases.

APPENDIX E: THE MINIMAL MODEL WITH DE NOVO AMP SYNTHESIS

Since the *E. coli* core model includes no AMP synthesis pathway, we assumed that the total concentration of the adenine nucleotide carriers (ATP, ADP, and AMP) is constant in the main text. To check if this assumption is crucial for the obtained result, we introduce a coarse-grained AMP synthesis reaction to the minimal model and study the dynamics of the model.

Here, we extend the minimal model studied in the main text. The nucleotide carriers such as AMP and GMP are synthesized from the pentose-phosphate pathway (PPP)
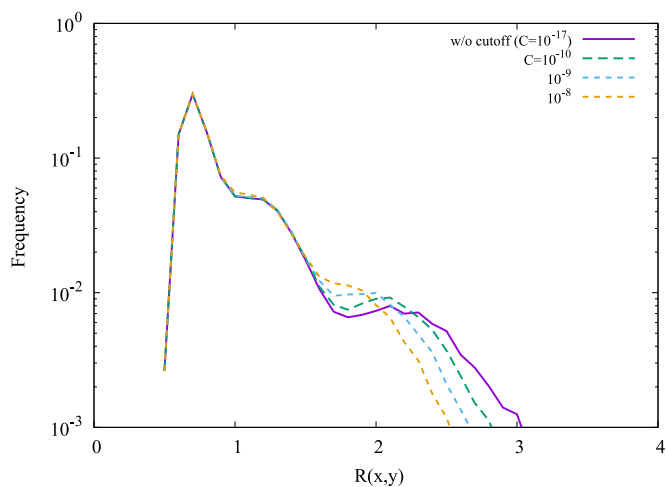
FIG. 10. The distribution of the expansion ratio of mode l0 with several values of cut-off: without cut-off (purple), $C = 10^{-10}$ (green), $C = 10^{-9}$ (cyan), and $C = 10^{-8}$ (orange). Parameters are set to the default values: $v = 1$ and $\kappa = 10^{-6}$ for all reactions, $[glc] = 1.0$, $A_t = 1.0$, $r = 0.1$, and $d = 10^{-8}$.

chemicals by utilizing ATP energy. In the minimal model, PPP is already removed from the model; thus, glucose is the chemical species closest to the PPP in the original metabolic network. Therefore, we introduced phenomenological AMP synthesis reaction glc + atp ⇌ amp + adp where glucose is the substrate, and the reaction needs the energy consumption (ATP → ADP). Then, the total concentration of adenine carriers is no longer constant, and thus, we put the constant-rate degradation term and the growth dilution term whose rate is
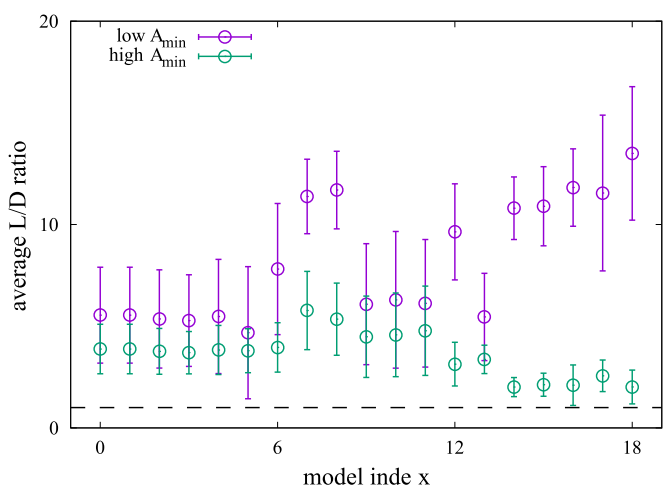

FIG. 11. The average ratio of the line integral of the trajectory (L) to the Euclidean distance between the initial point and the attractor (D) for the growth trajectories and dormant trajectory. The ratio L/D is averaged over the trajectories for each group (high and low A_{min} groups) and plotted against the model index with the error bars as the standard deviation. In all the cases, the low A_{min} trajectories have a larger L/D ratio than the growth trajectories. The broken-black line is an eye guideline representing $L/D = 1$.

proportional to the growth reaction to all chemicals. Then, the equations are given by

$$\frac{d[\text{pep}]}{dt} = J_{\text{uptake}} + J_{\text{pps}} - J_{\text{pyk}} - J_{\text{ppc}} - (d + \mu)[\text{pep}], \quad \text{(E1)}$$

$$\frac{d[\text{pyr}]}{dt} = J_{\text{pyk}} - J_{\text{pps}} - (d + \mu)[\text{pyr}], \quad \text{(E2)}$$

$$\frac{d[\text{oaa}]}{dt} = J_{\text{pps}} - J_{\text{growth}} - (d + \mu)[\text{oaa}], \quad \text{(E3)}$$

$$\frac{d[\text{atp}]}{dt} = J_{\text{uptake}} + J_{\text{pyk}} - J_{\text{pps}} - J_{\text{growth}} - J_{\text{adk1}}$$
$$- J_{\text{amps}} - (d + \mu)[\text{atp}], \quad \text{(E4)}$$

$$\frac{d[\text{adp}]}{dt} = -J_{\text{uptake}} - J_{\text{pyk}} + J_{\text{growth}} + 2J_{\text{adk1}}$$
$$+ J_{\text{amps}} - (d + \mu)[\text{adp}], \quad \text{(E5)}$$

$$\frac{d[\text{amp}]}{dt} = J_{\text{pps}} - J_{\text{akd1}} + J_{\text{amps}} - (d + \mu)[\text{amp}], \quad \text{(E6)}$$

$$J_{\text{amps}} = v_{\text{atp}}([\text{glc}][\text{atp}] - [\text{amp}][\text{adp}]). \quad \text{(E7)}$$

Here we analyzed the trajectories starting from randomly-generated initial point $10^{u_{i,n}}$ with $u_{i,n}$ as the uniformly-distributed random number in $[-1, 1]$ for the ith chemical and the nth initial point. This reduces the requirements of the computational resources because we can skip the computation for finding attractors. As far as we have checked, the model had a single attractor.

Figure 14 shows the distribution of the expansion ratio and the projected trajectories onto the two-dimensional PC space. As depicted, the model with the de-novo synthesis of AMP still exhibits distinct trajectories while the dormant trajectories become rare with the default parameter set.

APPENDIX F: MODEL0 WITH THE NICOTINAMIDE NUCLEOTIDE CARRIERS

In the main text, we replaced NAD(NADP) and NADH(NADPH) with ATP and ADP, respectively, with the assumption that the ATP synthesis via the electron transport chain and the conversion of NADP to NADPH is sufficiently quick. Here, we relax these assumptions and introduce the dynamics of NAD, NADH, NADP, and NADPH to model 0.

Here, we introduce two phenomenological reactions shown in Table I, and the replacement of the nicotinamide nucleotide carriers by the adenine nucleotide carriers is not performed. A full list of the reactions is provided in *SI Data*.3 within the Supplemental Material [42].

The reaction "ATPPMF" is for the ATP generation using proton motive force which consists of NADH16, CYTBD, and ATPS4r in the original core model. NADTRHD has the same stoichiometry as that in the core model except for the hydrogen ion.

In the model, the degradation and growth-dilution term are omitted for their dynamics, and [nad] + [nadh] and [nadp] + [nadph] are constant because the cofactors are not newly synthesized in the model. For simplicity, here we set [atp] + [adp] + [amp] = [nad] + [nadh] = [nadp] + [nadph] = A_t.
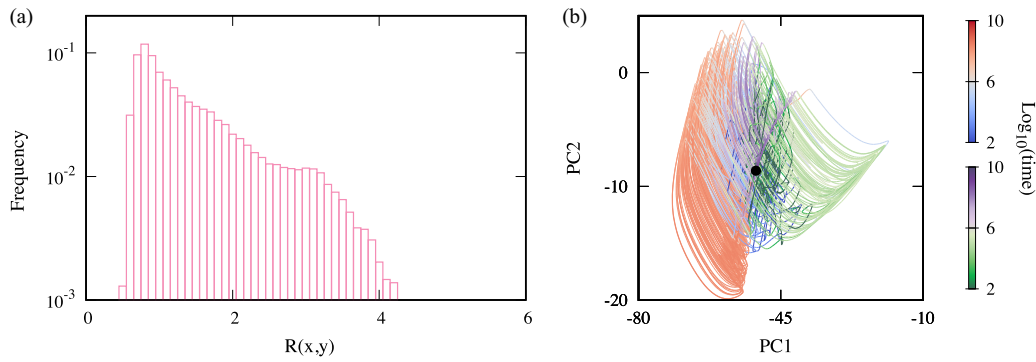
FIG. 12. (a) The distribution of the expansion ratio of the trajectories perturbed from the minor attractor. (b) The trajectories are projected onto the PC1-PC2 space. The trajectories are colored based on the dynamics of $A_{\min}$ (low: blue-white-red, high: green-white-purple). There are 145 growth and 160 dormant trajectories overlaid in the figure. Parameters are set to the default values: $v = 1$ and $\kappa = 10^{-6}$ for all reactions, $[\text{glc}] = 1.0$, $A_t = 1.0$, $r = 0.1$, and $d = 10^{-8}$.
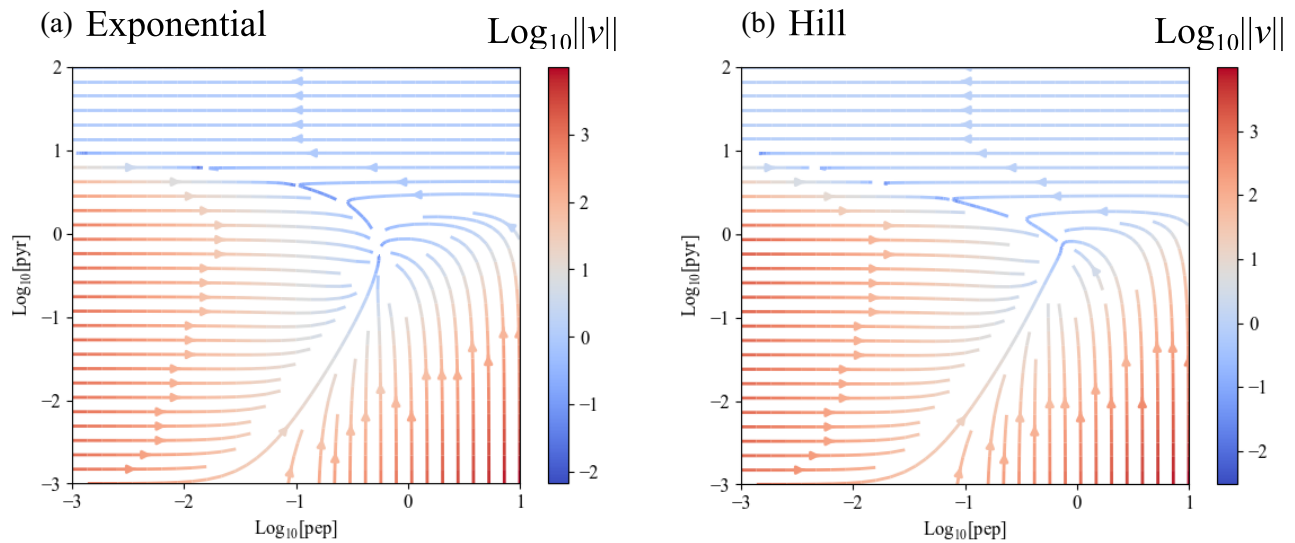

FIG. 13. The streamlines in the phase space with alternative functions. The exponential function $\exp(-[\text{pyr}])$ and the Hill function $[\text{pyr}]^{n_H}/(K^{n_H} + [\text{pyr}]^{n_H})$ are used as the function ϕ for (a) and (b), respectively. $K = 1.0$ and $n_H = -4$ for (b). The other parameter values are $v = 1$ and $\kappa = 10^{-6}$ for all reactions, $[\text{glc}] = 1.0$, $r = 0.1$, and $d = 10^{-8}$.
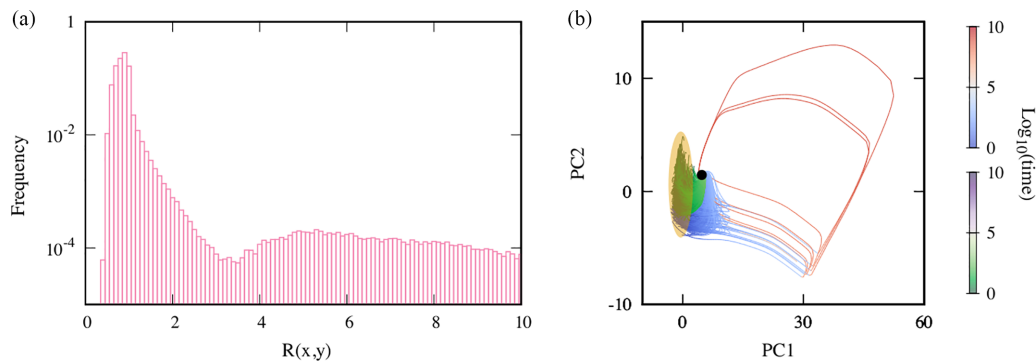

FIG. 14. (a) The distribution of the expansion ratio of the minimal model with the de novo AMP synthesis. It shows clear bimodality. (b) The trajectories projected onto the two-dimensional PC space. The green-white-purple and blue-white-red colored trajectories are the growth and the dormant trajectories, respectively. The trajectories are colored based on the relaxation time of each trajectory. The black dot represents the attractor and the initial points cluster in the region highlighted in orange. $v = 1$ and $\kappa = 10^{-6}$ for all reactions while $v_{\text{atp}} = 0.1$, $[\text{glc}] = 1.0$, $r = 0.1$, and $d = 10^{-8}$.

TABLE I. Reactions added to model 0.

Reaction name	Reaction formula
ATPPMF	$NADH + ADP \rightarrow NAD + ATP$
NADTRHD	$NAD + NADPH \rightarrow NADH + NADP$

Here we used the randomly-generated initial conditions with $u_{i,n}$ as the random number, $10^{u_{i,n}}$, $u_{i,n} \in [-1, 1]$, instead of the initial condition generated by the perturbation. The concentrations of the cofactors are normalized after assigning the random numbers. We found in this model the distinct trajectories emerge when the range of initial concentration of pyruvate is set to $[1, 10^3]$ (i.e, $u_{i,n} \in [0, 3]$ for pyruvate) as shown in Fig. 15. This is qualitatively consistent with the result of the minimal model in the main text that pyruvate plays a crucial role in displaying distinct relaxation behaviors. Including the nicotinamide nucleotide carries simply changes the needed pyruvate level to have a dormant trajectory quantitatively.

In this model, the separation of the trajectories is unclear in the two-dimensional PC space [Fig. 15(b)], while it is in the three-dimensional PC space [Fig. 15(c)]. Note that, in these figures, we colored the trajectories based on $A_{\min}$ because the distribution of $A_{\min}$ showed clear bimodality. However, it is not fully consistent with the separation of the trajectories in

Fig. 15(c). This is probably because $A_{\min}$ alone is now an insufficient indicator of the energetic state of the cell. For more precise coloring, the contributions of the nicotinamide nucleotide carriers should be incorporated, while it is beyond the scope of the present study.

APPENDIX G: MODEL REDUCTION WITH RANDOM ORDER

In the main text, We have obtained the minimal model by manually deciding the order of the reaction removal. However, in general, the resulting minimal models by the reduction depend on the order of the removal. Here, we reduce the *E. coli* core model in random order to investigate if the obtained minimal models share features in common with the one we presented in the main text.

Pseudocodes that summarize the algorithms are presented in the following. For the random reduction, we randomly choose a reaction and check if the reaction is removable by Algorithm 1 and iterate it until there is no more removable reaction.

Algorithm 1 requires the reaction network (a list of the reactions) and the name of the reaction to be removed as inputs. If the reaction is removable from the network, it returns the reaction network without the reaction, while it returns the same reaction network as the input if the reaction is not removable.
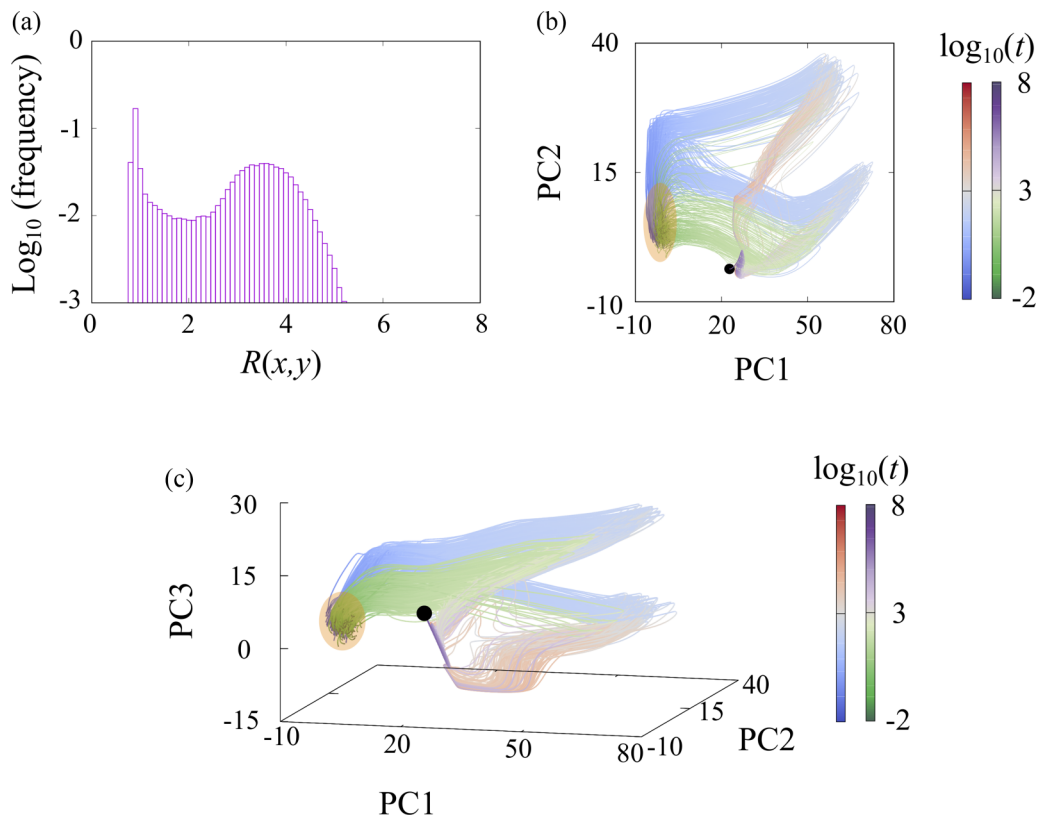

FIG. 15. (a) The distribution of the expansion ratio of the model 0 with NAD, NADH, NADP, and NADPH, showing clear bimodality. [(b),(c)] The trajectories in the two-dimensional (b) and three-dimensional (c) PC space. The green-white-purple and blue-white-red colored trajectories are the growth and the dormant trajectories, respectively. The trajectories are colored based on $A_{\min}$. The black dot represents the attractor and the initial points cluster in the region highlighted in orange. $v = 1$ and $\kappa = 10^{-6}$ for all reactions. Other parameters are $[glc] = 1.0$, $A_t = 1/3$, $r = 0.1$, and $d = 10^{-8}$.

Algorithm 1. Compute a reduced network from given network R and a reaction to be removed `rxn`.

Notations:

(i) R : the reaction network

(ii) B : the reaction network without ATP, ADP, and AMP

(iii) $R - T$: the reaction network without the reactions in T

(iv) $E(k)$: the number of reactions that the chemical k is associated

---

1: $C \leftarrow$ the list of chemicals in R

2: $C_0 \leftarrow C - $`'glc'`

3: **if** $E(k) \geqslant 2$ for $^\forall k \in C_0$ after `rxn` is removed **then**

4:     `RemoveList`←[`rxn`]

5:     `RenameList`←[]

6: **else if** `rxn` is one-to-one reaction in B **and** no loop b/w substrate and product of `rxn` **then**

7:     `RemoveList`←[`rxn`]

8:     `RenameList`←[(Substrate of `rxn`, Product of `rxn`)]

9: **else**

10:     find a minimal reaction set T so that $E(k) \geqslant 2$ or $E(k) = 0$ for $^\forall k \in C_0$ in $R - T$

11:     `RemoveList` ← T

12:     `RenameList`←[]

13: **end if**

14: $\tilde{R} \leftarrow R - $`RemoveList`

15: $\tilde{C} \leftarrow$ chemicals in $\tilde{R}$

16: Rename chemical names in $\tilde{R}$ and $\tilde{C}$ according to `RenameList`

17: **if** a growth factor g_i is removed **then**

18:     replace g_i by a closest chemical on B

19: **end if**

20: **if** Connected **and** Nonzero steady flux exists **and** The dist. of the exp. ratio is multimodal

21: **return** $\tilde{R}$

22: **else**

23: **return** R

24: **end if**

The algorithm first checks whether the input reaction can be simply removed (line 3) or the contraction is needed (line 6). In the case where the removal of the input reaction leads to dead-end chemicals (chemicals with only one reaction connected), the algorithm computes a set of reactions T. T is a minimal set of reactions, including the input reaction so the simultaneous removal of the reactions in T from the reaction network does not lead to dead-end chemicals (line 10).

If the reaction removal eliminates a chemical in the growth reaction, a neighboring chemical in the backbone network B (the reaction network without ATP, ADP, and AMP) is chosen as the replacement of the eliminated chemical (line $17-19$).

By removing the reaction, we obtain a candidate of the reduced reaction network $\tilde{R}$. Then, the algorithm checks if the network $\tilde{R}$ satisfies the following three conditions: connectivity, a nonzero steady flux without the degradation and growth dilution, and multimodality of the distribution of the expansion ratio (line 20).

Algorithm 2 calls Algorithm 1 with a randomly selected reaction(s) and checks if the obtained network is minimal.

To check if the distribution of the expansion ratio $\tilde{R}$ is multimodal and/or long tailed, we calculated $\tilde{R}$ of the kinetic model with a default parameter set used in the main text ($v = 1$ and $\kappa = 10^{-6}$ for all reactions).

Algorithm 2. The algorithm for a random reduction (the same notation with Algorithm 1 is used).

1: **while** 1 **do**

2:   `RxnList` $\leftarrow$ All reactions in $R-$['growth reaction']

3:   Shuffle `RxnList`

4:   **for** r in `RxnList` **do**

5:     $R_0 \leftarrow$ SingleLoopReduction(R, r) (*see Alg. 1*)

6:     **if** $R_0 \neq R$ **then**

7:     break

8:     **end if**

9:   **end for**

10:   **if** $R = R_0$ **then**

11:     **return** R

12:   **end if**

13:   $R \leftarrow R_0$

14: **end while**

The reaction lists of 16 minimal models obtained from different random seeds for the reduction are given in *SI Data.*4 within the Supplemental Material [42]. By random reduction, we obtained two groups of minimal models classified by the shape of the distribution of the expansion ratio. The first case shows clear multimodality (model #$0 - $#13). The second case shows a long tail rather than additional peaks (model #14 and #15), see Fig. 16.

All the minimal models had more reactions than the minimal model in the main text. Interestingly, the network structures of the minimal models are qualitatively different depending on whether the model exhibits the clear bimodal distribution of the expansion ratio or not. The models with the bimodal distribution share two network features, namely, (i) ATP, ADP, and AMP are in the model, and (ii) there are both types of reactions; with and without the adenine nucleotide carriers coupling as well as branching of the network. These are the vital network features for the model to satisfy the two conditions for the distinct trajectories discussed in the main text. We like to emphasize that during the random model reductions, several models without AMP were generated, while none of them showed a multimodal distribution of the expansion ratio, and they were rejected based on the distribution of the expansion ratio.

On the other hand, the minimal models exhibiting the distribution of the expansion ratio with a long tail lack the second condition, i.e., all the reactions are coupled with the adenine nucleotide carriers. As a consequence, all the metabolic reactions are uniformly slowed down even if ATP and ADP deplete. Thus, the distinction among the trajectories is not as clear as in the other minimal models.

In Fig. 17, we plotted the trajectories of each minimal model. Since we found that the distributions of $A_{\min}$ (see Appendix C 3) of the minimal models were double-peaked, we colored the trajectories by the same criterion used in Appendix C 3. Interestingly, there are several types of minimal models in terms of the visual impression of the trajectories in PC1-PC2 space; The minimal models show clear separations of two types of trajectories as the minimal model studied in the main text (#1, #2, #6 − #8, #11, and #12), models exhibiting the oscillation during the relaxation (#3 and #10), and
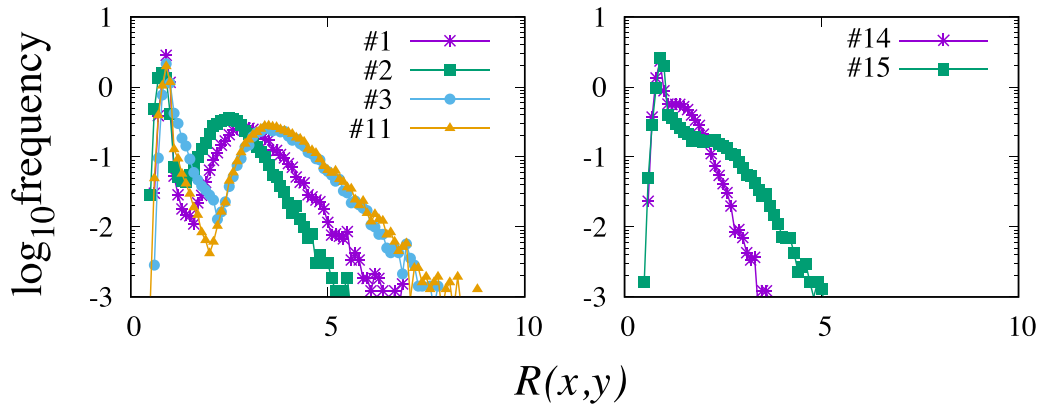
FIG. 16. Two types of resulted distribution of the expansion ratio. The first type exhibiting the clear multimodality (left) and the second type showing a long-tail rather than additional extrema (right). Labels in the panels are the indices of the minimal models.
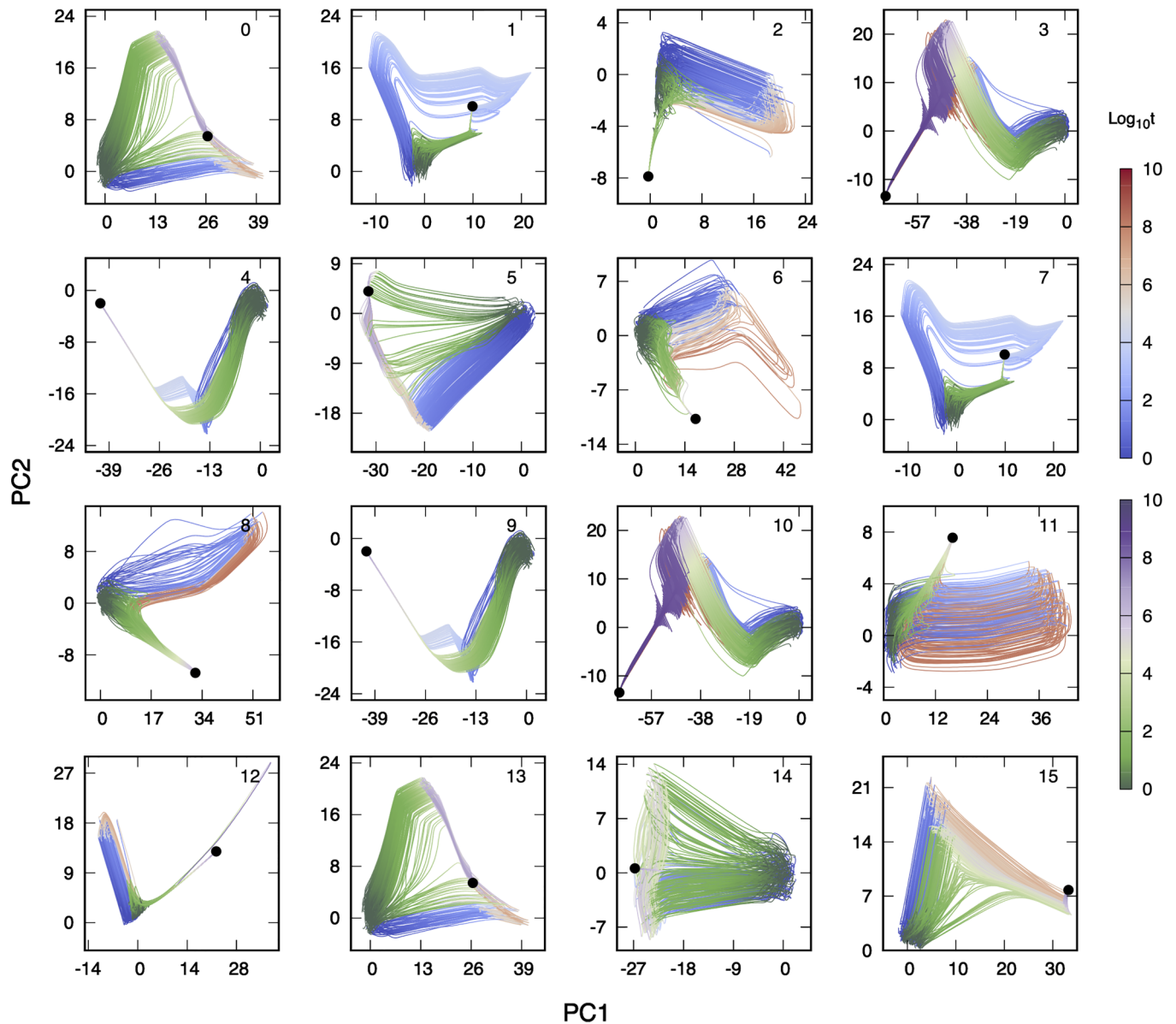

FIG. 17. The trajectories on the PCS. Trajectories are colored according to A_{min}.
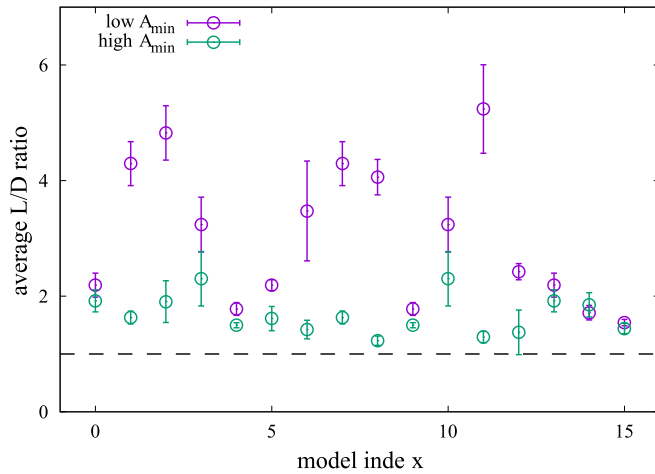
FIG. 18. The average L/D ratio of for the minimal models obtained by the random reduction. Error bars indicate the standard deviation. The trajectories with low A_{min} has a higher L/D ratio than that of trajectories with high A_{min}. The black-dashed line is $L/D = 1$ for an eye guide.
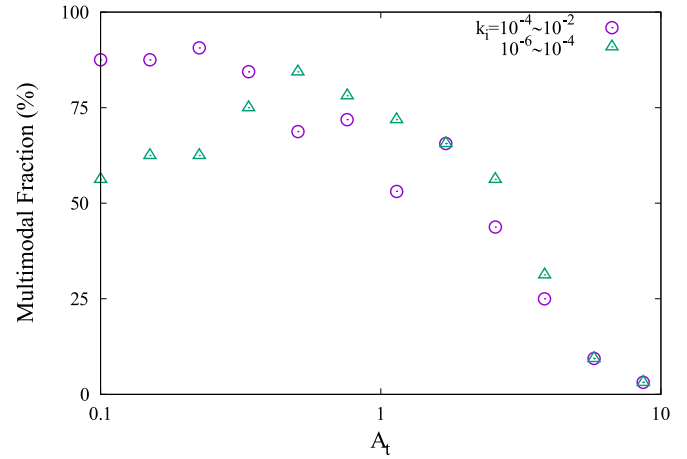

FIG. 19. The fraction of the parameter sets leading to a multimodal distribution of the expansion ratio is plotted as the function of the total adenine nucleotide carriers concentration A_t. The result obtained from the simulations with two different ranges of k_i's are overlaid.

models where the separation of the trajectories is not quite clear (#0, #4, #5, #9, and #13) [65]. However, in the original high-dimensional phase-space, the two types of trajectories are distinct in terms of the L/D ratio (see Sec. C 5) for the models with the bimodal distribution of the expansion ratio (model #0–#13) as shown in Fig. 18.

APPENDIX H: THE BEHAVIOR OF MODEL 0 WITH RANDOMLY ASSIGNED PARAMETERS

In the main text, we saw that the distinct trajectories emerge in two sets of parameter values, the realistic setting and uniform assignment for v_i's and k_i's. Here, we check the robustness of the emergence of the distinct trajectories by randomly assigning the parameter values.

We simulated model 0 with a variety of parameter values. As concluded in the main text, the concentrations of ATP and ADP play a crucial role in the emergence of distinct trajectories. Therefore, we studied the relaxation dynamics of the model with several values of the total concentrations of the adenine nucleotide carriers A_t (= [atp] + [adp] + [amp]). In addition, we assigned random values for the kinetic parameters in the rate equations [v_i's and k_i's. see Eq. (3) in the

main text]. We kept the concentration of the nutrient [glc], the degradation constant d, and the proportionality constant between the growth reaction and the growth rate r the same as the main text.

For each values of A_t, we generated 32 random vectors of parameters $\vec{p} = (\vec{v}, \vec{k})$ where $\vec{v}$ and $\vec{k}$ are vector representation of the parameters v_i's and k_i's, respectively. For each $\vec{p}$, we ran the differential equations from 128 randomly generated initial points and computed the distribution of the expansion ratio. v_i's and k_i's are given as 10^u where u is an uniformly-distributed random number. For v_i's, u ranges from 0 to 1, while it ranges from -6 to -4 or from -4 to -2 for k_i's.

Figure 19 shows the fraction of $\vec{p}$'s that led a bimodal distribution as a function of A_t. The results obtained from two different ranges of k_i's are overlaid. The bimodality is judged by using the same criterion described in Appendix C 2. The fraction of parameter sets leading to a bimodal distribution of the expansion ratio is a decreasing function of A_t if k_i's ranges from 10^{-4} to 10^{-2}, while interestingly, it shows non-monotonic behavior in the case where k_i's ranges from 10^{-6} to 10^{-4}. Thus, the emergence of distinct trajectories robustly takes place while the chance of it with random parameter assignments eventually decreases as A_t increases.

[1] G. Sezonov, D. Joseleau-Petit, and R. d'Ari, *Escherichia coli* physiology in Luria-Bertani broth, J. Bacteriol. **189**, 8746 (2007).

[2] N. Q. Balaban, J. Merrin, R. Chait, L. Kowalik, and S. Leibler, Bacterial persistence as a phenotypic switch, Science **305**, 1622 (2004).

[3] N. Q. Balaban, S. Helaine, K. Lewis, M. Ackermann, B. Aldridge, D. I. Andersson, M. P. Brynildsen, D. Bumann, A. Camilli, J. J. Collins *et al.*, Definitions and guidelines for research on antibiotic persistence, Nat. Rev. Microbiol. **17**, 441 (2019).

[4] S. K. Christensen, M. Mikkelsen, K. Pedersen, and K. Gerdes, Rele, a global inhibitor of translation, is activated during nutritional stress, Proc. Natl. Acad. Sci. USA **98**, 14328 (2001).

[5] Y. Himeoka and N. Mitarai, When to wake up? The optimal waking-up strategies for starvation-induced persistence, PLoS Comput. Biol. **17**, e1008655 (2021).

[6] M. S. Svenningsen, S. L. Svenningsen, M. A. Sørensen, and N. Mitarai, Existence of log-phase *Escherichia coli* persisters and lasting memory of a starvation pulse, Life Sci. Alliance **5**, e202101076 (2022).

[7] I. Levin-Reisman, O. Gefen, O. Fridman, I. Ronin, D. Shwa, H. Sheftel, and Nathalie Q. Balaban, Automated imaging with scanlag reveals previously undetectable bacterial growth phenotypes, Nat. Methods **7**, 737 (2010).

[8] Y. Himeoka and K. Kaneko, Theory for Transitions between Exponential and Stationary Phases: Universal Laws for Lag Time, Phys. Rev. X **7**, 021049 (2017).

[9] Y. Himeoka, B. Gummesson, M. A. Sørensen, S. L. Svenningsen, and N. Mitarai, Distinct survival, growth lag, and rRNA degradation kinetics during long-term starvation for carbon or phosphate, mSphere **7**, e0100621 (2022).

[10] E. Biselli, S. J. Schink, and U. Gerland, Slower growth of *Escherichia coli* leads to longer survival in carbon starvation due to a decrease in the maintenance rate, Mol. Syst. Biol. **16**, e9478 (2020).

[11] J. L. Radzikowski, S. Vedelaar, D. Siegel, Á. D. Ortega, A. Schmidt, and M. Heinemann, Bacterial persistence is an active σs stress response to metabolic flux limitation, Mol. Syst. Biol. **12**, 882 (2016).

[12] S. M. Amato, C. H. Fazen, T. C. Henry, W. W. K. Mok, M. A. Orman, E. L. Sandvik, K. G. Volzing, and M. P. Brynildsen, The role of metabolism in bacterial persistence, Front. Microbiol. **5**, 70 (2014).

[13] J. L. Radzikowski, H. Schramke, and M. Heinemann, Bacterial persistence from a system-level perspective, Curr. Opin. Biotechnol. **46**, 98 (2017).

[14] S. Klumpp, Z. Zhang, and T. Hwa, Growth rate-dependent global effects on gene expression in bacteria, Cell **139**, 1366 (2009).

[15] I. Golding, J. Paulsson, S. M. Zawilski, and E. C. Cox, Real-time kinetics of gene activity in individual bacteria, Cell **123**, 1025 (2005).

[16] K. Fujita, M. Iwaki, and T. Yanagida, Transcriptional bursting is intrinsically caused by interplay between RNA polymerases on DNA, Nat. Commun. **7**, 13788 (2016).

[17] A. Awazu and K. Kaneko, Ubiquitous "glassy" relaxation in catalytic reaction networks, Phys. Rev. E **80**, 041931 (2009).

[18] A. Awazu and K. Kaneko, Discreteness-induced slow relaxation in reversible catalytic reaction networks, Phys. Rev. E **81**, 051920 (2010).

[19] T. S. Hatakeyama and C. Furusawa, Metabolic dynamics restricted by conserved carriers: Jamming and feedback, PLoS Comput. Biol. **13**, e1005847 (2017).

[20] C. Chassagnole, N. Noisommit-Rizzi, J. W. Schmid, K. Mauch, and M. Reuss, Dynamic modeling of the central carbon metabolism of escherichia coli, Biotechnol. Bioeng. **79**, 53 (2002).

[21] H. Kurata and Y. Sugimoto, Improved kinetic model of *Escherichia coli* central carbon metabolism in batch and continuous cultures, J. Biosci. Bioeng. **125**, 251 (2018).

[22] T. A. A. Kadir, A. A. Mannan, A. M. Kierzek, J. McFadden, and K. Shimizu, Modeling and simulation of the main metabolism in *Escherichia coli* and its several single-gene knockout mutants with experimental verification, Microb. Cell Factories **9**, 1 (2010).

[23] Y. Tohsato, K. Ikuta, A. Shionoya, Y. Mazaki, and M. Ito, Parameter optimization and sensitivity analysis for large kinetic models using a real-coded genetic algorithm, Gene **518**, 84 (2013).

[24] O. Kotte, J. B. Zaugg, and M. Heinemann, Bacterial adaptation through distributed sensing of metabolic fluxes, Mol. Syst. Biol. **6**, 355 (2010).

[25] K. Peskov, E. Mogilevskaya, and O. Demin, Kinetic modelling of central carbon metabolism in *Escherichia coli*, FEBS J. **279**, 3374 (2012).

[26] A. A. Mannan, Y. Toya, K. Shimizu, J. McFadden, A. M. Kierzek, and A. Rocco, Integrating kinetic model of *E. coli* with genome scale metabolic fluxes overcomes its open system problem and reveals bistability in central metabolism, PLoS One **10**, e0139507 (2015).

[27] J. Di Maggio, J. C. D. Ricci, and M. S. Diaz, Global sensitivity analysis in dynamic metabolic networks, Comput. Chem. Eng. **26**, 1075 (2010).

[28] K. Bettenbrock, S. Fischer, A. Kremling, K. Jahreis, T. Sauter, and E.-D. Gilles, A quantitative approach to catabolite repression in *Escherichia coli*, J. Biol. Chem. **281**, 2578 (2006).

[29] V. K. Singh and I. Ghosh, Kinetic modeling of tricarboxylic acid cycle and glyoxylate bypass in mycobacterium tuberculosis, and its application to assessment of drug targets, Theor. Biol. Med. Model. **3**, 1 (2006).

[30] C. J. Torres, V. Guixé, and J. Babul, A mutant phosphofructokinase produces a futile cycle during gluconeogenesis in *Escherichia coli*, Biochem. J. **327**, 675 (1997).

[31] Y. Tan and J. C. Liao, Metabolic ensemble modeling for strain engineers, Biotechnol. J. **7**, 343 (2012).

[32] L. M. Tran, M. L. Rizk, and J. C. Liao, Ensemble modeling of metabolic networks, Biophys. J. **95**, 5606 (2008).

[33] A. Khodayari, A. R. Zomorrodi, J. C. Liao, and C. D. Maranas, A kinetic model of *Escherichia coli* core metabolism satisfying multiple sets of mutant flux data, Metab. Eng. **25**, 50 (2014).

[34] A. Khodayari and C. D. Maranas, A genome-scale escherichia coli kinetic metabolic model k-ecoli457 satisfying flux data for multiple mutant strains, Nat. Commun. **7**, 1 (2016).

[35] M. L. Rizk and J. C. Liao, Ensemble modeling for aromatic production in *Escherichia coli*, PLoS One **4**, e6903 (2009).

[36] S. Manuse, Y. Shan, S. J. Canas-Duarte, S. Bakshi, W.-S. Sun, H. Mori, J. Paulsson, and K. Lewis, Bacterial persisters are a stochastically formed subpopulation of low-energy cells, PLoS Biol. **19**, e3001194 (2021).

[37] B. P. Conlon, S. E. Rowe, A. B. Gandt, A. S. Nuxoll, N. P. Donegan, E. A. Zalis, G. Clair, J. N. Adkins, A. L. Cheung, and K. Lewis, Persister formation in *Staphylococcus aureus* is associated with ATP depletion, Nat. Microbiol. **1**, 16051 (2016).

[38] Y. Shan, A. B. Gandt, S. E. Rowe, J. P. Deisinger, B. P. Conlon, and K. Lewis, ATP-dependent persister formation in *Escherichia coli*, MBio **8**, 1 (2017).

[39] F. Pedregosa, G. Varoquaux, A. Gramfort, V. Michel, B. Thirion, O. Grisel, M. Blondel, P. Prettenhofer, R. Weiss, V. Dubourg *et al.*, Scikit-learn: Machine learning in Python, J. Machine Learn. Res. **12**, 2825 (2011).

[40] J. D. Orth, R. M. T. Fleming, B. Ø. Palsson, *Reconstruction and Use of Microbial Metabolic Networks: The Core Escherichia coli Metabolic Model as an Educational Guide*, 2010.

[41] Z. A. King, A. Dräger, A. Ebrahim, N. Sonnenschein, N. E. Lewis, and B. O. Palsson, Escher: A web application for building, sharing, and embedding data-rich visualizations of biological pathways, PLoS Comput. Biol. **11**, e1004321 (2015).

[42] See Supplemental Material at http://link.aps.org/supplemental/10.1103/PhysRevResearch.4.043223 for the reaction list and

parameter values of the realistic model, and the structure of the minimal models obtained by the random order.

[43] The concentration of glutamine [the purple bottommost line in the top panel of Fig. 2(a)] reached unrealistically low value even in the steady state. We attribute this behavior to the following technical reason: The biomass synthesis reaction was not incorporated into the model in [33] where the kinetic parameters were estimated. In the present model, we added the biomass synthesis reaction to consider the cell growth, which resulted in much faster consumption of glutamine than in the model used for parameter estimate. See Appendix A.

[44] This is not necessary for the argument, but makes the equation complicated.

[45] D. Shah, Z. Zhang, A. Khodursky, N. Kaldalu, K. Kurg, and K. Lewis, Persisters: A distinct physiological state of *E. coli*, BMC Microbiol. **6**, 53 (2006).

[46] S. B. Korch and T. M. Hill, Ectopic overexpression of wild-type and mutant hipA genes in *Escherichia coli*: Effects on macromolecular synthesis and persister formation, J. Bacteriol. **188**, 3826 (2006).

[47] E. Rotem, A. Loinger, I. Ronin, I. Levin-Reisman, C. Gabay, N. Shoresh, O. Biham, and N. Q. Balaban, Regulation of phenotypic variability by a threshold-based mechanism underlies bacterial persistence, Proc. Natl. Acad. Sci. USA **107**, 12541 (2010).

[48] A. Rocco, A. M. Kierzek, and J. McFadden, Slow protein fluctuations explain the emergence of growth phenotypes and persistence in clonal bacterial populations, PLoS One **8**, e54272 (2013).

[49] I. Cataudella, K. Sneppen, K. Gerdes, and N. Mitarai, Conditional cooperativity of toxin-antitoxin regulation can mediate bistability between growth and dormancy, PLoS Comput. Biol. **9**, e1003174 (2013).

[50] L. Gelens, L. Hill, A. Vandervelde, J. Danckaert, and R. Loris, A general model for toxin-antitoxin module dynamics can explain persister cell formation in *E. coli*, PLoS Comput. Biol. **9**, e1003190 (2013).

[51] J. Feng, D. A. Kessler, E. Ben-Jacob, and H. Levine, Growth feedback as a basis for persister bistability, Proc. Natl. Acad. Sci. USA **111**, 544 (2014).

[52] D. Nguyen, A. Joshi-Datar, F. Lepine, E. Bauerle, O. Olakanmi, K. Beer, G. McKay, R. Siehnel, J. Schafhauser, Y. Wang, B. E. Britigan, and P. K. Singh, Active starvation responses mediate antibiotic tolerance in biofilms and nutrient-limited bacteria, Science **334**, 982 (2011).

[53] V. Hauryliuk, G. C. Atkinson, K. S. Murakami, T. Tenson, and K. Gerdes, Recent functional insights into the role of (p)ppgpp in bacterial physiology, Nat. Rev. Microbiol. **13**, 298 (2015).

[54] R. Hengge-Aronis, Signal transduction and regulatory mechanisms involved in control of the σs (rpos) subunit of RNA polymerase, Microbiol. Mol. Biol. Rev. **66**, 373 (2002).

[55] R.v. Lange and R. Hengge-Aronis, Identification of a central regulator of stationary-phase gene expression in *Escherichia coli*, Mol. Microbiol. **5**, 49 (1991).

[56] R. Page and W. Peti, Toxin-antitoxin systems in bacterial growth arrest and persistence, Nat. Chem. Biol. **12**, 208 (2016).

[57] P. Sharma, P. P. Pandey, and S. Jain, Modeling the cost and benefit of proteome regulation in a growing bacterial cell, Phys. Biol. **15**, 046005 (2018).

[58] R. Patnaik, W. D. Roof, R. F. Young, and J. C. Liao, Stimulation of glucose catabolism in *Escherichia coli* by a potential futile cycle, J. Bacteriol. **174**, 7527 (1992).

[59] O. Hädicke, K. Bettenbrock, and S. Klamt, Enforced atp futile cycling increases specific productivity and yield of anaerobic lactate production in escherichia coli, Biotechnol. Bioeng. **112**, 2195 (2015).

[60] M. Kanehisa and S. Goto, Kegg: Kyoto encyclopedia of genes and genomes, Nucleic Acids Res. **28**, 27 (2000).

[61] C. M. Bishop, *Pattern Recognition and Machine Learning*, (Springer, New York, 2006).

[62] L. Gerosa, B. R. B. H. van Rijsewijk, D. Christodoulou, K. Kochanowski, T. S. B. Schmidt, E. Noor, and U. Sauer, Pseudo-transition analysis identifies the key regulators of dynamic metabolic adaptations from steady-state data, Cell Sys. **1**, 270 (2015).

[63] A. Akbari, J. T. Yurkovich, D. C. Zielinski, and B. O. Palsson, The quantitative metabolome is shaped by abiotic constraints, Nat. Commun. **12**, 3178 (2021).

[64] A. Cornish-Bowden, *Fundamentals of Enzyme Kinetics* (John Wiley & Sons, Hoboken, NJ, 2013).

[65] Note that the reductions were made in random order and the same minimal network can result. Actually, there are several the same model pairs, namely, #0 and #13, #1 and #7, #3 and #10 and #4 and #9.